Available online at www.sciencedirect.com
ScienceDirect
Computers and Mathematics with Applications 55 (2008) 23–50
An International Journal
computers & mathematics
with applications
www.elsevier.com/locate/camwa

Adaptive kernel estimation and SPH tensile instability

Leonardo Di G. Sigalotti [a,*], Hender López [a,b]

[a] *Centro de Física, Instituto Venezolano de Investigaciones Científicas, IVIC, Apartado Postal 21827, Caracas 1020A, Venezuela*
[b] *Departament d'Enginyeria Electrónica, Universitat Autònoma de Barcelona, 08193 Bellaterra, Barcelona, Spain*

Received 1 November 2005; received in revised form 1 December 2006; accepted 20 March 2007

Abstract

We propose an alternative method to remove the tensile instability in standard SPH simulations of a fluid. The method relies on an *adaptive density kernel estimation* (ADKE) algorithm, which allows the width of the kernel interpolant to vary locally in such a way that only the minimum necessary smoothing is applied to the data. By means of a linear perturbation analysis of the SPH equations for a heat-conducting, viscous, van der Waals fluid, we derive the corresponding dispersion relation. Solution of the dispersion relation in the short wavelength limit shows that the tensile instability is effectively removed for a wide range of the ADKE parameters. Application of the method to the formation of equilibrium liquid drops confirms the analytical results of the linear stability analysis. Examples of the resolving power of the method are also given for the nonlinear oscillations of an excited drop and the Sedov blast wave problem.

Keywords: Particle methods; Stability; Kernel functions; Numerical-methods; Fluid dynamics

1. Introduction

It is well known that in numerical simulations of elastic solids with the method of Smoothed Particle Hydrodynamics (SPH), the SPH particles may tend to clump in pairs under tension. This instability was first studied by Schüssler and Schmitt [1] in the context of gas dynamics and by Phillips and Monaghan [2] in the context of magnetohydrodynamics. Later on, Swegle et al. [3] performed a detailed analysis of the instability for their model calculations of deforming elastic solids, and dubbed it *tensile* instability. They found that it is due to an effective stress with a negative modulus (i.e., imaginary sound speed), resulting from the interaction between the interpolating kernel function and the equation of state. In applications to solids, the SPH particles mimic the behavior of the atoms. That is, if the solid is compressed, the atoms repel each other, while if it is stretched, they attract each other and oppose the stretching. The same occurs for the SPH particles, except that, when the solid is stretched, the applied strains amplify as particle-to-particle fluctuations due to noise frequency growing with time. Therefore, the attraction results in a clumping of the SPH particles toward stable configurations. As noticed by Swegle et al. [3], the instability is related to the sign of both the stress and the second derivative of the kernel function. A compressive stress (i.e., a negative

* Corresponding author. Tel.: +58 0212 5041369; fax: +58 0212 5041148.
E-mail addresses: lsigalot@cassini.ivic.ve (L. Di G. Sigalotti), hlopez@ivic.ve (H. López).

0898-1221/$ - see front matter
doi:10.1016/j.camwa.2007.03.007

stress) corresponds to ordinary molecular dynamics, with the kernel playing the role of a smooth repulsive potential. In contrast, a tensile stress (i.e., a positive stress) corresponds to a purely attractive potential, and leads to instability. Thus neighboring particles tend to clump together, exponentially fast at first, when the local stress is tensile rather than compressive.

The tensile instability is also known to occur in fluids [1]. Clear evidence for unstable behavior in fluids is given by Nugent and Posch [4], who reported SPH calculations of the formation and evaporation of liquid drops. The appearance of a well-defined pattern, consisting of alternating concentric dense rings of particles and voids in their final equilibrium drops, is a clear symptom of artificial clustering due to the tensile instability. A number of methods have been proposed to eliminate it from SPH simulations. In particular, Monaghan [5] found that for isotropic fluids, the tensile instability can be removed by adding to the pressure-gradient acceleration a short-range artificial force between the particles. Using a linear perturbation analysis of the SPH Euler equations, he derived the form of this repulsive force in the short wavelength limit. This same analysis was further generalized to the case of stressed solid bodies by Gray et al. [6]. Their method adds an artificial stress to the governing SPH equations modelled on the artificial repulsive force. Since the differential equations describing the dynamics of deformable elastic bodies have the same structure as those describing the motion of viscous fluids, the artificial stress derived by Gray et al. [6] for an elastic solid can be applied to viscous fluids, provided that the constant parameter involved in the definition of the artificial stress is properly chosen [7].

An alternative method for removing the tensile instability was suggested by Dyka et al. [8], which relies on the inclusion of an additional set of stress nodes at points other than the SPH particle locations. Since the stress particles do not carry a velocity, a moving least square estimate is needed for their movement [9]. However, this method is computationally expensive in multi-dimensions, because the stress points have to be tracked for each SPH element in the course of the calculation. Other existing methods that relieve the suffering from the tensile instability involve corrections of the kernel estimates that exactly reproduce linear functions [10–13]. In particular, Dilts [10] showed that the tensile instability can be significantly reduced by generalizing SPH through the use of an interpolant which gives accurate derivatives regardless of the positions of the particles. In addition, a corrective SPH method was implemented by Chen et al. [11], in which a Taylor series expansion up to second-order terms is used to construct the corrective kernel estimate. However, when this method is applied to multi-dimensions, a matrix inversion is required to get each individual derivative estimate. Although these corrective techniques are by far more accurate than standard SPH, they involve substantially more work, so that even if they remove the tensile instability, they may not be competitive with other schemes. Furthermore, Belytschko and Xiao [14] studied the stability of particle methods based on the Shepard function with corrected derivatives. They considered both Eulerian and Lagrangian kernels with nodal integration, as in standard SPH, and stress point stabilization, as proposed by Dyka et al. [8]. They realized that the tensile instability originates as a distortion of the material instability induced by Eulerian kernels, and that a Lagrangian kernel with the addition of stress points effectively eliminates it. In a recent paper, Hoover et al. [15] showed that the unstable exponential growth of kinetic energy associated with tension in standard SPH disappears when Monaghan's [16] velocity averaging is used. Since one effect of the velocity averaging is to decrease the relative velocity of approach of neighboring particles, Hoover et al. [15] found that when this procedure is applied to a rotating compressible elastic disk, the symptoms of tensile instability are delayed for nearly a complete rotation period of the disk.

In this paper, we report an alternative method to avoid the tensile instability in fluid-dynamic SPH simulations. Unlike standard SPH, the present scheme is based on an *adaptive density kernel estimation* (ADKE) algorithm similar to that described by Silverman [17]. This method combines intrinsic features of both the kernel and nearest neighbor approaches, in a way that the amount of smoothing applied to the data is effectively controlled. The basic idea lies in constructing an estimate consisting of a collection of local bandwidth factors, or kernels, placed at the location of particles in order to allow the final smoothing length of the kernel to vary from point to point. The definition of the local bandwidth factors involves two constant parameters, which can be conveniently chosen to reduce, or even eliminate, the tensile instability. Through a linear analysis of the SPH equations, we derive the corresponding dispersion relation and solve it in the short wavelength limit to obtain the dependence of the frequency on the local bandwidth factor. The solution of the dispersion relation predicts that the tensile instability is effectively removed for a wide range of the ADKE parameters. We apply the method to a heat-conducting, viscous liquid with a van der Waals equation of state, and show that the ADKE method produces numerically stable results that agree with the predictions of our linear analysis. For a single choice of the ADKE parameters, the method is also seen to perform well for more

dynamical test problems, including the large-amplitude oscillations of an elliptically deformed drop and the Sedov blast wave problem [18].

2. The equations for a viscous fluid with heat conduction

The differential equations describing the dynamics of a heat-conducting, viscous fluid are: (a) the continuity equation

$$\frac{\mathrm{d}\rho}{\mathrm{d}t} = -\rho\frac{\partial v^j}{\partial x^j}, \tag{1}$$

(b) the acceleration equation

$$\rho\frac{\mathrm{d}v^i}{\mathrm{d}t} = \frac{\partial S^{ij}}{\partial x^j}, \tag{2}$$

and (c) the thermal energy equation

$$\rho\frac{\mathrm{d}U}{\mathrm{d}t} = S^{ij}\frac{\partial v^i}{\partial x^j} - \frac{\partial q^j}{\partial x^j}, \tag{3}$$

where $\mathrm{d}/\mathrm{d}t = \partial/\partial t + v^i\partial/\partial x^i$ is the Lagrangian time derivative, ρ is the density, v^i is the ith component of the fluid velocity, U is the specific internal energy, x^j is the jth Cartesian component of the position vector, S^{ij} is the stress tensor, and q^j is the jth component of the heat flux vector. The stress tensor can be written as

$$S^{ij} = -p\delta^{ij} + \sigma^{ij}, \tag{4}$$

where p is the internal pressure, δ^{ij} is the unit tensor, and σ^{ij} is the viscous stress tensor given by

$$\sigma^{ij} = \eta\left(\frac{\partial v^i}{\partial x^j} + \frac{\partial v^j}{\partial x^i}\right) + \left(\zeta - \frac{2}{d}\eta\right)\frac{\partial v^k}{\partial x^k}\delta^{ij}, \tag{5}$$

where η and ζ are the coefficients of shear and bulk viscosity, respectively, and $d = 2$ for two-dimensional flow and $d = 3$ for three-dimensional motion. We assume that the heat flux obeys Fourier's law

$$q^j = -\kappa\frac{\partial T}{\partial x^j}, \tag{6}$$

where T is the fluid temperature and κ is the coefficient of heat conduction.

Eqs. (1)–(3) must be closed with constitutive relations for the pressure and specific internal energy. Here we assume a van der Waals fluid, and define

$$p = \frac{\rho\bar{k}_{\mathrm{B}}T}{1-\rho\bar{b}} - \bar{a}\rho^2, \tag{7}$$

and

$$U = \frac{\xi}{2}\bar{k}_{\mathrm{B}}T - \bar{a}\rho, \tag{8}$$

where ξ is the number of degrees of freedom of the molecules, $\bar{k}_{\mathrm{B}} = k_{\mathrm{B}}/m$, $\bar{b} = b/m$, $\bar{a} = a/m^2$, k_{B} is Boltzmann's constant, b is a constant due to the finite size of the molecules, a is the cohesive action responsible for the short-range attractive forces between neighboring molecules, and m is the mass of the molecules.

3. The SPH equations

In SPH simulations, the density at the location of particle "a" is computed in either of the two ways: (a) using the summation interpolant

$$\rho_a = \sum_{b=1}^{N} m_b W_{ab}, \tag{9}$$

where the summation includes the contribution of particle "a" itself, or (b) using the SPH analog of the continuity equation

$$\frac{\mathrm{d}\rho_a}{\mathrm{d}t} = \sum_{b=1}^{N} m_b \left(v_a^j - v_b^j\right) \frac{\partial W_{ab}}{\partial x_a^j}. \tag{10}$$

The two forms are identical provided that the initial densities used in Eq. (10) are chosen to match the summed-up values given by Eq. (9). Here $W_{ab} = W(|\mathbf{x}_a - \mathbf{x}_b|, h)$ is the kernel (or weight) function, and h is the smoothing length, which is a measure of the size of the kernel support. The summations in Eqs. (9) and (10) are over all particles, though in practice only near neighbors contribute, because the kernel W_{ab} has a finite range.

The SPH acceleration equation corresponding to Eq. (2) is

$$\frac{\mathrm{d}v_a^i}{\mathrm{d}t} = \sum_{b=1}^{N} m_b \left(\frac{S_a^{ij}}{\rho_a^2} + \frac{S_b^{ij}}{\rho_b^2}\right) \frac{\partial W_{ab}}{\partial x_a^j}, \tag{11}$$

whereas the SPH representation of the thermal energy equation (3) is

$$\frac{\mathrm{d}U_a}{\mathrm{d}t} = \frac{1}{2}\sum_{b=1}^{N} m_b \left(\frac{S_a^{ij}}{\rho_a^2} + \frac{S_b^{ij}}{\rho_b^2}\right)\left(v_b^i - v_a^i\right) \frac{\partial W_{ab}}{\partial x_a^j} - \sum_{b=1}^{N} m_b \left(\frac{q_a^j}{\rho_a^2} + \frac{q_b^j}{\rho_b^2}\right) \frac{\partial W_{ab}}{\partial x_a^j}, \tag{12}$$

where a summation over the index j is implied on the right-hand side of Eq. (11), and similarly, over the indices i and j in Eq. (12). In addition to the above SPH equations, we must also solve the equation

$$\frac{\mathrm{d}x_a^i}{\mathrm{d}t} = v_a^i, \tag{13}$$

to evolve the particle positions.

According to the analysis of Bonet and Lok [19], if the symmetrized SPH forms given by Eqs. (11) and (12) are used to evolve the velocity and thermal energy of the particles, then the variational consistency of the whole scheme would demand using Eq. (9) rather than Eq. (10) for calculating the density. Though typical formulations of SPH preserve mass, linear momentum, and energy, angular momentum is in general not conserved by SPH. For a conservative system, the interpolations inherent to the discrete SPH representation of the continuous field causes an error of order h^2 for the time derivative of the total angular momentum [15]. This error persists even if variational consistency is ensured. Moreover, the viscous stresses contributed by σ^{ij} are noncentral forces in Eq. (2), and so they violate the conservation law for the total angular momentum. This problem was studied by Nugent and Posch [4], who considered the dynamics of rotating, circular drops with the same SPH formulation given by Eqs. (9)–(13). In particular, they found that angular momentum decreases exponentially in time with a decay time that varies as $1/h^2$. Thus, if a full Newtonian stress tensor is used, angular momentum is conserved only to order h, and the decay time is proportional to $1/\eta$. The accuracy and stability of standard SPH can be significantly improved if the smoothing is based on an adaptive density kernel estimation (ADKE) procedure as described by Silverman [17]. This class of estimate combines intrinsic features of both the kernel and nearest neighbor approaches in such a way that the amount of smoothing required in low-density regions is minimized. The basic idea is to construct an estimate consisting of a collection of kernels placed at the positions of the particles in order to allow the bandwidth (or smoothing length) to vary from point to point. This is easily accomplished by first computing an initial, or *pilot*, density estimate using the summation interpolant in Eq. (9) as

$$\hat{\rho}_a = \sum_{b=1}^{N} m_b W(|\mathbf{x}_a - \mathbf{x}_b|, h_0), \tag{14}$$

where h_0 is defined as some dilation factor D of the initial uniform interparticle separation Δs, i.e., $h_0 = D\Delta s$. Local bandwidth factors, λ_a, are next constructed according to the relation

$$\lambda_a = \beta \left(\frac{\hat{\rho}_a}{\bar{g}} \right)^{-\varepsilon}, \tag{15}$$

where $\bar{g}$ is the geometric mean of the pilot estimates defined as

$$\ln \bar{g} = \frac{1}{N} \sum_{b=1}^{N} \log \hat{\rho}_b, \tag{16}$$

β is a constant scaling factor on the order of unity, and ε is the so-called sensitivity parameter defined in the interval $0 \leq \varepsilon \leq 1$. As a final step, the adaptive estimator is obtained by defining the width of the kernel at the location of particle "a" as $h_a = \lambda_a h_0$, and by recalculating the density using Eq. (14) with h_0 replaced by h_a. Note that for $\varepsilon \to 1$, the local bandwidth factors will become more sensitive to variations in the pilot density distribution, implying a greater difference between the smoothing lengths, h_a, in different parts of the sample. On the other hand, setting $\varepsilon = 0$ will bring the method back to the fixed width kernel approach, provided that $\beta = 1$ in Eq. (15). In order to ensure the conservation of linear momentum and total energy, the actual kernel estimate is symmetrized with respect to particle pairs by replacing h_a by the average mean [20]

$$h_{ab} = \frac{1}{2} (h_a + h_b) \tag{17}$$

so that the kernel employed in Eqs. (9)–(12) to evolve the density, velocity, and thermal energy of the particles is

$$W_{ab} = W(|\mathbf{x}_a - \mathbf{x}_b|, h_{ab}). \tag{18}$$

With the values of λ_a calculated in this way, the h_a's effectively control the scale of the smoothing applied to the data. This aspect improves the accuracy and stability of standard SPH. In particular, it was found to give good results for strong shocks and rarefactions [21]. Here we show that the ADKE method can also remove the tensile instability for a wide range of λ_a.

The ADKE procedure results in a resolution varying SPH scheme that differs from other adaptive SPH formulations in common use, where a changing smoothing length is enforced either by allowing the h_a's to vary with the density according to the relation $h_a \sim (m_a/\rho_a)^{1/d}$, with d being the number of dimensions [22,23], or by relating the time rate of change of h to that of the density at each observation point via the differential equation $\mathrm{d} \ln h/\mathrm{d}t = -(1/d)\mathrm{d} \ln \rho/\mathrm{d}t$ [20,24]. An alternative procedure was introduced by Monaghan [25], in which the h_a's are determined directly from the summation for the density

$$\rho_a = \sum_b m_b W_{ab}(h_a).$$

This equation gives the density as a nonlinear function of h, which in turn can be used to solve h iteratively in terms of the local density by means of any standard root-finding algorithm. A viable procedure to do so is to use the density at the previous timestep as a first estimate. The value of h calculated in this way is then consistent with the density obtained from the summation. A similar consistency is embodied by the ADKE prescriptions (14)–(16), but without the need for iterating. The use of Eq. (14) for the pilot density estimate makes it to be sensitive to the same sort of scale as the final adaptive estimate through Eq. (15). In other words, provided that the kernel function W is nonnegative, the ADKE procedure will be effectively a *bonafide* probability density. The crucial point is that it will not suffer from the excessively heavy tails as the nearest neighbor method does, because only the minimum necessary smoothing will be applied to regions of low density.

4. The exact dispersion relation

In order to compare with the SPH dispersion relation, we first perform a linear perturbation analysis of Eqs. (1)–(8) and derive the corresponding dispersion relation, assuming that the unperturbed state is a uniform, infinite fluid at rest.

To do so we use Cartesian coordinates and represent the flow in the (x, y)-plane. Linearization of the above equations is obtained by perturbing the initial state with small Fourier variations of the form

$$\begin{aligned}
&\begin{pmatrix} x \\ y \end{pmatrix} = \begin{pmatrix} x_0 \\ y_0 \end{pmatrix} + \begin{pmatrix} X \\ Y \end{pmatrix} \mathrm{e}^{\mathrm{i}(\mathbf{k}\cdot\mathbf{r}_0 - \omega t)}, \\
&\begin{pmatrix} v_x \\ v_y \end{pmatrix} = \begin{pmatrix} V_x \\ V_y \end{pmatrix} \mathrm{e}^{\mathrm{i}(\mathbf{k}\cdot\mathbf{r}_0 - \omega t)}, \\
&\rho = \rho_0 + \bar{\rho}, \\
&\bar{\rho} = \mathcal{D}\mathrm{e}^{\mathrm{i}(\mathbf{k}\cdot\mathbf{r}_0 - \omega t)}, \\
&T = T_0 + \bar{T}, \\
&\bar{T} = \mathcal{T}\mathrm{e}^{\mathrm{i}(\mathbf{k}\cdot\mathbf{r}_0 - \omega t)}, \\
&p = p_0 + c_0^2\bar{\rho} + \frac{\bar{k}_\mathrm{B}}{(1 - \bar{b}\rho_0)}\bar{T}, \\
&U = U_0 + \bar{k}_\mathrm{B}\bar{T} - \bar{a}\bar{\rho},
\end{aligned} \tag{19}$$

where the unperturbed quantities are shown by the subscript "0", and their variation by overbars. Here c_0 is the sound speed given by

$$c_0^2 = \frac{\bar{k}_\mathrm{B} T_0}{(1 - \bar{b}\rho_0)^2} - 2\bar{a}\rho_0, \tag{20}$$

$\mathbf{k} = (k_x, k_y)$ is the wave vector, ω is the wave frequency, and $\mathbf{r}_0 = (x_0, y_0)$ is the initial position vector. We further assume that the velocity perturbation is always subsonic, that is, much less than the speed of sound. In this van der Waals fluid model, the perturbed and unperturbed temperatures and densities must satisfy the constraints $\bar{k}_\mathrm{B} T > 2\bar{a}\rho(1 - \bar{b}\rho)^2$ and $\rho < 1/\bar{b}$ for thermodynamic stability. The first inequality guarantees the positiveness of the isentropic bulk modulus, $K_s = \rho(\partial p/\partial\rho)_s$, and therefore ensures that the sound speed will be a real quantity. The second inequality guarantees that the kinetic pressure, given by the first term in Eq. (7), is always positive. The sign of the pressure will then be determined by the balance between the cohesive and kinetic pressures. Note that in writing the variation of the thermal energy in Eq. (19), we have taken $\xi = 2$ in Eq. (8), as it is appropriate for spherical molecules that are allowed to move only in the (x, y)-plane.

Substitution of the above expressions into the continuity equation (1) yields the linearized relation

$$\omega\mathcal{D} = \rho_0 (\mathbf{k}\cdot\mathbf{V}) = \rho_0 \left(k_x V_x + k_y V_y\right). \tag{21}$$

Similarly, the x- and y-components of the acceleration equation (2) become

$$\omega\rho_0 V_x = c_0^2 k_x \mathcal{D} + \frac{k_x \mathcal{T}\bar{k}_\mathrm{B}\rho_0}{(1 - \bar{b}\rho_0)} - \mathrm{i}\left[(\eta + \zeta)\, k_x^2 V_x + \eta k_y^2 V_x + \zeta k_x k_y V_y\right], \tag{22}$$

and

$$\omega\rho_0 V_y = c_0^2 k_y \mathcal{D} + \frac{k_y \mathcal{T}\bar{k}_\mathrm{B}\rho_0}{(1 - \bar{b}\rho_0)} - \mathrm{i}\left[(\eta + \zeta)\, k_y^2 V_y + \eta k_x^2 V_y + \zeta k_x k_y V_x\right], \tag{23}$$

respectively, while the thermal energy equation (3) takes the form

$$\omega\rho_0 \left(\bar{k}_\mathrm{B}\mathcal{T} - \bar{a}\mathcal{D}\right) = p_0 \left(k_x V_x + k_y V_y\right) - \mathrm{i}\kappa\mathcal{T}\left(k_x^2 + k_y^2\right). \tag{24}$$

Since viscous heating contributes to the thermal energy with second-order terms, no viscous terms appear in the above linearized equation.

4.1. Case in which $\eta = \zeta = 0$ and $\kappa = 0$

In the absence of viscous and heat-conductive effects, Eq. (21) remains unaltered, while Eqs. (22)–(24) become

$$\begin{aligned}
\omega\rho_0 V_x &= c_0^2 k_x \mathcal{D} + \frac{k_x \mathcal{T} \bar{k}_{\mathrm{B}} \rho_0}{(1 - \bar{b}\rho_0)}, \\
\omega\rho_0 V_y &= c_0^2 k_y \mathcal{D} + \frac{k_y \mathcal{T} \bar{k}_{\mathrm{B}} \rho_0}{(1 - \bar{b}\rho_0)}, \\
\frac{\omega\rho_0}{p_0} &= \frac{\bar{k}_{\mathrm{B}} \mathcal{T} - \bar{a}\mathcal{D}}{k_x V_x + k_y V_y}.
\end{aligned} \tag{25}$$

From the first two equations it follows that $V_x/V_y = k_x/k_y$, which represents a longitudinal wave in which $\mathbf{V} \propto \mathbf{k}$. Combining the last relation with Eq. (21) yields $\mathcal{T}/T_0 = (\mathcal{D}/\rho_0)/(1 - \bar{b}\rho_0)$. Thus $\mathcal{T} = 0$ only if $\mathcal{D} = 0$, in which case $V_x/V_y = -k_y/k_x$, which represents a complete transverse wave. Hence, transverse waves are not responsible for inducing density or temperature variations in the fluid.

4.2. Limit when κ is large

We shall derive the exact dispersion relation in the limit when κ is sufficiently large, so that waves propagate at essentially constant temperature. Solving for $\mathcal{T}$ in Eq. (24) and using Eq. (7), we find that

$$\frac{\mathcal{T}}{T_0} = \frac{\omega\mathcal{D}\bar{k}_{\mathrm{B}}(\omega\rho_0\bar{k}_{\mathrm{B}} - \mathrm{i}\kappa k^2)}{(1 - \bar{b}\rho_0)(\omega^2\bar{k}_{\mathrm{B}}^2\rho_0^2 + \kappa^2 k^4)}, \tag{26}$$

where $k^2 = k_x^2 + k_y^2$. In the limit, when $\kappa \to \infty$ we find that $\mathcal{T} \to 0$. Hence, wave-induced temperature fluctuations are efficiently eradicated when the thermal conductivity is high enough. Multiplying Eq. (26) by κ and taking again the limit when $\kappa \to \infty$ gives

$$\kappa\mathcal{T}|_{\kappa\to\infty} = -\frac{\mathrm{i}\omega\mathcal{D}\bar{k}_{\mathrm{B}} T_0}{(1 - \bar{b}\rho_0)k^2}. \tag{27}$$

Substitution of this limiting form into Eq. (24) leads to the unperturbed van der Waals equation of state. Thus, in the limit of large κ, when $\mathcal{T} \to 0$, Eq. (24) is satisfied identically, and our set of linearized equations (21)–(24) reduces to

$$\begin{aligned}
&\omega\mathcal{D} - \rho_0 k_x V_x - \rho_0 k_y V_y = 0, \\
&k_x c_0^2 \mathcal{D} - \{\omega\rho_0 + \mathrm{i}[(\eta + \zeta)k_x^2 + \eta k_y^2]\}V_x - \mathrm{i}\zeta k_x k_y V_y = 0, \\
&k_y c_0^2 \mathcal{D} - \mathrm{i}\zeta k_x k_y V_x - \{\omega\rho_0 + \mathrm{i}[(\eta + \zeta)k_y^2 + \eta k_x^2]\}V_y = 0.
\end{aligned} \tag{28}$$

A non-trivial solution of these equations can be obtained by demanding that the determinant of the coefficients vanish, which leads to the dispersion relation

$$\rho_0^2\omega^3 + \mathrm{i}(\zeta + 2\eta)\rho_0 k^2\omega^2 - k^2[c_0^2\rho_0^2 + \eta(\eta + \zeta)k^2]\omega - \mathrm{i}\eta c_0^2\rho_0 k^4 = 0, \tag{29}$$

which is a cubic complex polynomial whose solution gives the frequency as a function of the wavenumber. Note that the above polynomial can also be solved for $k = k(\omega)$, in which case it will be quadratic in k^2.

5. The SPH dispersion relation

As in Gray et al. [6], we assume for simplicity that the SPH particles are placed at the vertices of a regular Cartesian grid such that they are separated from each other by a distance Δs along the x- and y-directions. Then, the mass of each particle is simply $\rho_0(\Delta s)^2$. As for the continuum case, we use a Fourier representation of the perturbed variables. If we denote by $\mathbf{r}_{0,a} = (x_{0,a}, y_{0,a})$ the initial position of particle "a", its perturbed position $\mathbf{r}_a = (x_a, y_a)$ is

$$\begin{pmatrix} x_a \\ y_a \end{pmatrix} = \begin{pmatrix} x_{0,a} \\ y_{0,a} \end{pmatrix} + \begin{pmatrix} X \\ Y \end{pmatrix} \mathrm{e}^{\mathrm{i}(\mathbf{k}\cdot\mathbf{r}_{0,a} - \omega t)}. \tag{30}$$

If we further assume that the particles are initially at rest, the perturbed velocity of particle "a", $\mathbf{v}_a = (v_{xa}, v_{ya})$, takes the form

$$\begin{pmatrix} v_{xa} \\ v_{ya} \end{pmatrix} = \begin{pmatrix} V_x \\ V_y \end{pmatrix} \mathrm{e}^{\mathrm{i}(\mathbf{k}\cdot\mathbf{r}_{0,a}-\omega t)}. \tag{31}$$

As for the position and velocity, the remainder of the perturbed variables associated with particle a are denoted by the subscript "a", and they take the same form as in Eq. (19), with the subscript "0" replaced by "$0, a$" and with $\mathbf{k}\cdot\mathbf{r}_0$ replaced by $\mathbf{k}\cdot\mathbf{r}_{0,a}$.

Substitution of Eqs. (30) and (31) into Eq. (13) yields the simple linearized relations

$$\omega X = \mathrm{i}V_x, \tag{32}$$

$$\omega Y = \mathrm{i}V_y. \tag{33}$$

We now introduce the definitions

$$\begin{aligned}
A_{x,a} &= (\Delta s)^2 \sum_{b=1}^{N} \sin(\mathbf{k}\cdot\mathbf{r}_{0,ab}) \frac{\partial W_{ab}}{\partial x_{0,a}}, \\
A_{y,a} &= (\Delta s)^2 \sum_{b=1}^{N} \sin(\mathbf{k}\cdot\mathbf{r}_{0,ab}) \frac{\partial W_{ab}}{\partial y_{0,a}}, \\
B_{x,a} &= (\Delta s)^2 \sum_{b=1}^{N} \cos(\mathbf{k}\cdot\mathbf{r}_{0,ab}) \frac{\partial W_{ab}}{\partial x_{0,a}}, \\
B_{y,a} &= (\Delta s)^2 \sum_{b=1}^{N} \cos(\mathbf{k}\cdot\mathbf{r}_{0,ab}) \frac{\partial W_{ab}}{\partial y_{0,a}}, \\
C_x &= (\Delta s)^2 \sum_{b=1}^{N} [1-\cos(\mathbf{k}\cdot\mathbf{r}_{0,ab})] \frac{\partial^2 W_{ab}}{\partial x_{0,a}^2}, \\
C_y &= (\Delta s)^2 \sum_{b=1}^{N} [1-\cos(\mathbf{k}\cdot\mathbf{r}_{0,ab})] \frac{\partial^2 W_{ab}}{\partial y_{0,a}^2}, \\
C_{xy} &= (\Delta s)^2 \sum_{b=1}^{N} [1-\cos(\mathbf{k}\cdot\mathbf{r}_{0,ab})] \frac{\partial^2 W_{ab}}{\partial x_{0,a}\partial y_{0,a}},
\end{aligned} \tag{34}$$

along with the double summations

$$F_{xx} = (\Delta s)^2 \sum_{b=1}^{N} [B_{x,b}\cos(\mathbf{k}\cdot\mathbf{r}_{0,ab}) - A_{x,b}\sin(\mathbf{k}\cdot\mathbf{r}_{0,ab})] \frac{\partial W_{ab}}{\partial x_{0,a}}, \tag{35}$$

$$F_{xy} = (\Delta s)^2 \sum_{b=1}^{N} [B_{x,b}\cos(\mathbf{k}\cdot\mathbf{r}_{0,ab}) - A_{x,b}\sin(\mathbf{k}\cdot\mathbf{r}_{0,ab})] \frac{\partial W_{ab}}{\partial y_{0,a}}, \tag{36}$$

$$F_{yx} = (\Delta s)^2 \sum_{b=1}^{N} [B_{y,b}\cos(\mathbf{k}\cdot\mathbf{r}_{0,ab}) - A_{y,b}\sin(\mathbf{k}\cdot\mathbf{r}_{0,ab})] \frac{\partial W_{ab}}{\partial x_{0,a}}, \tag{37}$$

$$F_{yy} = (\Delta s)^2 \sum_{b=1}^{N} [B_{y,b}\cos(\mathbf{k}\cdot\mathbf{r}_{0,ab}) - A_{y,b}\sin(\mathbf{k}\cdot\mathbf{r}_{0,ab})] \frac{\partial W_{ab}}{\partial y_{0,a}}, \tag{38}$$

where the quantities

$$A_{x,b} = (\Delta s)^2 \sum_{c=1}^{N} \sin(\mathbf{k}\cdot\mathbf{r}_{0,bc}) \frac{\partial W_{bc}}{\partial x_{0,b}},$$

$$A_{y,b} = (\Delta s)^2 \sum_{c=1}^{N} \sin(\mathbf{k}\cdot\mathbf{r}_{0,bc}) \frac{\partial W_{bc}}{\partial y_{0,b}},$$

$$B_{x,b} = (\Delta s)^2 \sum_{c=1}^{N} \cos(\mathbf{k}\cdot\mathbf{r}_{0,bc}) \frac{\partial W_{bc}}{\partial x_{0,b}},$$

$$B_{y,b} = (\Delta s)^2 \sum_{c=1}^{N} \cos(\mathbf{k}\cdot\mathbf{r}_{0,bc}) \frac{\partial W_{bc}}{\partial y_{0,b}},$$

have to be distinguished from those in Eq. (34) in that the former represent summations over the nearest neighbors of particle "b", which is itself a neighbor of the reference particle "a". The double summations arise as a consequence of the SPH discretization of the spatial second derivatives of the velocity implied in the definition of the viscous acceleration terms on the right-hand side of Eq. (11). Susbstituting the perturbed variables into Eqs. (10)–(12), the continuity equation takes the form

$$\omega\mathcal{D} = -\rho_0(A_{x,a}V_x + A_{y,a}V_y), \tag{39}$$

while the x- and y-components of the SPH acceleration equation become

$$\begin{aligned}\omega\rho_0 V_x = {} & \frac{2p_0}{\omega}(C_x V_x + C_{xy}V_y) - \left[\frac{1}{\rho_0}(c_0^2\rho_0 - 2p_0)\mathcal{D} + \frac{\bar{k}_{\mathrm{B}}\rho_0\mathcal{T}}{(1-\bar{b}\rho_0)}\right]A_{x,a} \\ & + \mathrm{i}[(\eta+\zeta)F_{xx}V_x + (\zeta-\eta)F_{yx}V_y + \eta(F_{yy}V_x + F_{xy}V_y)],\end{aligned} \tag{40}$$

and

$$\begin{aligned}\omega\rho_0 V_y = {} & \frac{2p_0}{\omega}(C_{xy} V_x + C_y V_y) - \left[\frac{1}{\rho_0}(c_0^2\rho_0 - 2p_0)\mathcal{D} + \frac{\bar{k}_{\mathrm{B}}\rho_0\mathcal{T}}{(1-\bar{b}\rho_0)}\right]A_{y,a} \\ & + \mathrm{i}[(\eta+\zeta)F_{yy}V_y + (\zeta-\eta)F_{xy}V_x + \eta(F_{yx}V_x + F_{xx}V_y)],\end{aligned} \tag{41}$$

respectively. Finally, the thermal energy equation reduces to

$$\omega\rho_0(\bar{k}_{\mathrm{B}}\mathcal{T} - \bar{a}\mathcal{D}) = -p_0(A_{x,a}V_x + A_{y,a}V_y) + \mathrm{i}\kappa\mathcal{T}(F_{xx} + F_{yy}). \tag{42}$$

As in the continuum case, when κ is sufficiently large $\mathcal{T} \to 0$. In addition, solving for $\kappa\mathcal{T}$ in Eq. (42) and taking the limit when $\kappa \to \infty$ gives

$$\kappa\mathcal{T}|_{\kappa\to\infty} = -\frac{\mathrm{i}\omega\bar{k}_{\mathrm{B}}\mathcal{D}T_0}{(1-\bar{b}\rho_0)(F_{xx}+F_{yy})}, \tag{43}$$

which, when replaced back into Eq. (42) leads, after a simple algebra, to the van der Waals equation of state for the unperturbed field. Thus, under the assumption of large thermal conductivity, Eq. (42) is satisfied automatically and so our set of linearized SPH equations reduces to

$$\begin{aligned}&\omega\mathcal{D} + \rho_0 A_{x,a}V_x + \rho_0 A_{y,a}V_y = 0, \\ &\omega(c_0^2\rho_0 - 2p_0)A_{x,a}\mathcal{D} + \rho_0\{\omega^2\rho_0 - 2p_0C_x - \mathrm{i}\omega[(\eta+\zeta)F_{xx} + \eta F_{yy}]\}V_x \\ &\quad - \rho_0\{2p_0C_{xy} + \mathrm{i}\omega[(\zeta-\eta)F_{yx} + \eta F_{xy}]\}V_y = 0, \\ &\omega(c_0^2\rho_0 - 2p_0)A_{y,a}\mathcal{D} - \rho_0\{2p_0C_{xy} + \mathrm{i}\omega[(\zeta-\eta)F_{xy} + \eta F_{yx}]\}V_x \\ &\quad + \rho_0\{\omega^2\rho_0 - 2p_0C_y - \mathrm{i}\omega[(\eta+\zeta)F_{yy} + \eta F_{xx}]\}V_y = 0.\end{aligned} \tag{44}$$

Using the first of these equations in the last two to eliminate $\mathcal{D}$, and making the definitions

$$\begin{aligned}
\alpha_{xx} &= \frac{1}{\rho_0}\left[(\eta+\zeta)F_{xx}+\eta F_{yy}\right],\\
\alpha_{xy} &= \frac{1}{\rho_0}\left[\eta F_{xy}+(\zeta-\eta)F_{yx}\right],\\
\alpha_{yx} &= \frac{1}{\rho_0}\left[\eta F_{yx}+(\zeta-\eta)F_{xy}\right],\\
\alpha_{yy} &= \frac{1}{\rho_0}\left[(\eta+\zeta)F_{yy}+\eta F_{xx}\right],\\
\gamma_{xx} &= 2\frac{p_0}{\rho_0}C_x+\left(c_0^2-2\frac{p_0}{\rho_0}\right)A_{x,a}^2,\\
\gamma_{xy} &= 2\frac{p_0}{\rho_0}C_{xy}+\left(c_0^2-2\frac{p_0}{\rho_0}\right)A_{x,a}A_{y,a},\\
\gamma_{yy} &= 2\frac{p_0}{\rho_0}C_y+\left(c_0^2-2\frac{p_0}{\rho_0}\right)A_{y,a}^2,
\end{aligned} \tag{45}$$

the remaining two equations can be manipulated to give the dispersion relation

$$\begin{aligned}
&\omega^4-\mathrm{i}(\alpha_{xx}+\alpha_{yy})\omega^3-(\gamma_{xx}+\gamma_{yy}+\alpha_{xx}\alpha_{yy}-\alpha_{xy}\alpha_{yx})\omega^2\\
&\quad+\mathrm{i}[\alpha_{xx}\gamma_{yy}+\alpha_{yy}\gamma_{xx}-\gamma_{xy}(\alpha_{xy}+\alpha_{yx})]\omega+(\gamma_{xx}\gamma_{yy}-\gamma_{xy}^2)=0,
\end{aligned} \tag{46}$$

which is a quartic complex polynomial relating the frequency to the wavenumber. In contrast, the exact dispersion relation given by Eq. (29) is cubic in ω. This is so because in the continuum limit, the term

$$\gamma_{xx}\gamma_{yy}-\gamma_{xy}^2\to 0,$$

exactly. The response to small perturbations is unstable if the imaginary part of ω is positive; that is, if $\mathrm{Im}(\omega)>0$. In this case, the perturbations, once having arisen, will grow indefinitely with time. Conversely, the response is stable either if the perturbations decay exponentially with time, in which case $\mathrm{Im}(\omega)<0$, or remain constant in amplitude [$\mathrm{Im}(\omega)=0$]. In addition, a response is expected to be asymptotically stable if it decays to zero as time goes to infinity.

5.1. Limit of long wavelengths

In the limit, when $k=\sqrt{k_x^2+k_y^2}$ is small enough and the smoothing length h is much larger than the interparticle separation, the summations in Eqs. (34)–(38) can be approximated by integrals. To do so, we first define the Fourier transform of the kernel W as

$$\begin{aligned}
\tilde{W}(k) &= \frac{1}{\sqrt{2\pi}}\int_{-\infty}^{+\infty}W(\mathbf{r})\mathrm{e}^{\mathrm{i}\mathbf{k}\cdot\mathbf{r}}\mathrm{d}\mathbf{r}\\
&= \frac{1}{\sqrt{2\pi}}\int_{-\infty}^{+\infty}W(\mathbf{r})\cos(\mathbf{k}\cdot\mathbf{r})\mathrm{d}\mathbf{r}+\mathrm{i}\frac{1}{\sqrt{2\pi}}\int_{-\infty}^{+\infty}W(\mathbf{r})\sin(\mathbf{k}\cdot\mathbf{r})\mathrm{d}\mathbf{r}\\
&= \tilde{W}_c+\mathrm{i}\tilde{W}_s.
\end{aligned} \tag{47}$$

It then follows that the Fourier transforms of ∇W and $\nabla^2 W$, say $\tilde{\mathbf{G}}$ and $\tilde{L}$, obey the relations

$$\tilde{\mathbf{G}}=\frac{1}{\sqrt{2\pi}}\int_{-\infty}^{+\infty}\nabla W(\mathbf{r})\mathrm{e}^{\mathrm{i}\mathbf{k}\cdot\mathbf{r}}\mathrm{d}\mathbf{r}=\mathbf{k}\tilde{W}_s-\mathrm{i}\mathbf{k}\tilde{W}_c, \tag{48}$$

and

$$\tilde{L}=\frac{1}{\sqrt{2\pi}}\int_{-\infty}^{+\infty}\nabla^2 W(\mathbf{r})\mathrm{e}^{\mathrm{i}\mathbf{k}\cdot\mathbf{r}}\mathrm{d}\mathbf{r}=-k^2\tilde{W}_c-\mathrm{i}k^2\tilde{W}_s, \tag{49}$$

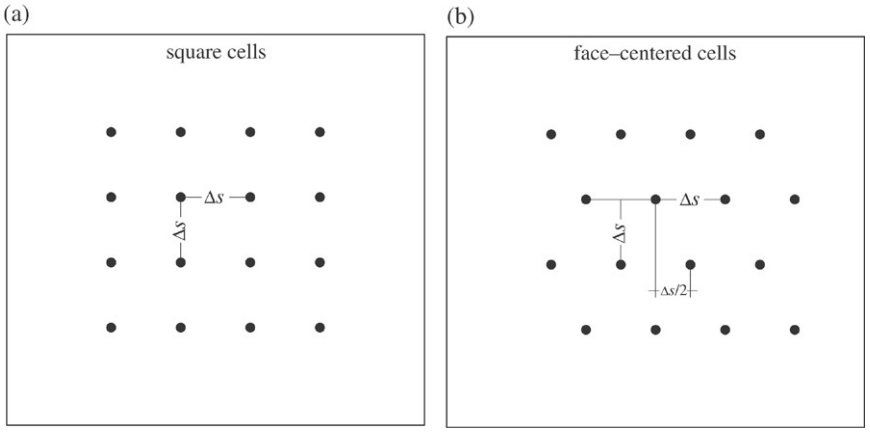

Fig. 1. Positions of SPH particles in two-dimensional meshes: (a) square cell array and (b) face-centered lattice.

respectively. Therefore, we find from Eqs. (34)–(38) that

$$\begin{aligned}
&\mathbf{A}_{x,a} = (A_{x,a}, A_{y,a}) \to -\mathbf{k}\tilde{W}_c,\\
&\mathbf{B}_{x,a} = (B_{x,a}, B_{y,a}) \to \mathbf{k}\tilde{W}_s,\\
&C_x \to k_x^2 \tilde{W}_c,\\
&C_y \to k_y^2 \tilde{W}_c,\\
&C_{xy} \to k_x k_y \tilde{W}_c,\\
&F_{xx} \to k_x^2 \left(\tilde{W}_s^2 - \tilde{W}_c^2\right),\\
&F_{xy} \to k_x k_y \left(\tilde{W}_s^2 - \tilde{W}_c^2\right),\\
&F_{yx} \to F_{xy},\\
&F_{yy} \to k_y^2 \left(\tilde{W}_s^2 - \tilde{W}_c^2\right),
\end{aligned} \tag{50}$$

where we have used the fact that $\mathbf{A}_{x,b} \to -\mathbf{k}\tilde{W}_c$ and $\mathbf{B}_{x,b} \to \mathbf{k}\tilde{W}_s$.

If we use the above equivalences into the SPH linearized equations (39)–(42), and note that in the limit when $k \to 0$, $\tilde{W}_c \to 1$ and $\tilde{W}_s \to 0$, we recover the linearized continuum equations (21)–(24). This result implies that the SPH linearized equations are correct in the long wavelength limit, and that the dispersion introduced by the SPH discretization can be determined from the Fourier transform of the kernel.

5.2. Limit of short wavelengths

It is well known that the SPH tensile instability is a short wavelength instability, initially involving the clumping of particles in pairs [5]. The rate of growth of the instability depends on the initial distribution of the particles, the kernel function, the value of h, and the equation of state. In particular, Belytschko and Xiao [14] showed that Eulerian kernels, (i.e., those which are functions of the spatial Eulerian coordinates), as they are customarily used in SPH calculations, are not able to replicate accurately the material instability. According to their analysis, the tensile instability arises as a manifestation of error in the reproduction of the material instability by Eulerian kernels. Conversely, Lagrangian kernels, which are functions of the material coordinates, reproduce the onset of material instability exactly. However, for the purposes of the present analysis, we shall consider an Eulerian kernel with nodal integration along with a van der Waals equation of state. We apply the analysis to various sizes of h and to two initial particle distributions, corresponding to the cases in which: (a) the particles are placed at the vertices of a regular Cartesian mesh composed of square cells each of side Δs, as shown in Fig. 1(a), and (b) the particles are on a grid where each horizontal line is made up of particles spaced by Δs, except that every second line is shifted in the x-direction by $\Delta s/2$ to form a face centered lattice, as depicted in Fig. 1(b).

In all cases, we shall only consider waves propagating along the x-axis, with

$$k_x = \frac{\pi}{\Delta s}, \qquad k_y = 0. \tag{51}$$

We recall that the dangerous modes are the longitudinal ones, with $V_x \neq 0$ and $V_y = 0$, because if they are unstable, then clumping occurs. On the contrary, pure transverse modes, with $V_x = 0$ and $V_y \neq 0$, if they amplify, they result in lines of particles moving vertically very slowly.

There is no a simple general approximation to the dispersion relation in the limit of short wavelengths. However, following an analysis similar to that given by Monaghan [5], for the case of inviscid fluids, and by Gray et al. [6], for elastic solids, we can get useful information by evaluating the summations involved in the coefficients of Eq. (46) for $h_0 = D\Delta s$, with $D \leq 5$, so that only nearest and next nearest neighbors contribute to the summations. In the ADKE method, the actual width of the kernel at the location of particle "a" is $h_a = h_0\lambda_a$, with the λ_a's as defined by Eqs. (15) and (16). In the present analysis, we shall consider values of $D = 2$, 2.5, 3, 3.5, 4, 4.5, and 5 along with the quartic spline kernel proposed by Lucy [26], which in two-dimensions reads as follows

$$W(r,h) = \frac{5}{\pi h^2}\begin{cases}(1+3q)(1-q)^3 & \text{if } 0 \leq q < 1,\\ 0 & \text{if } q \geq 1,\end{cases} \tag{52}$$

where $q = r/h$ and $r = \sqrt{x^2+y^2}$ in Cartesian coordinates. The reason for choosing this kernel is that it has recently been used in problems of liquid drop formation [4,7] and studies of the tensile instability in elastic solids [15].

6. Stability analysis

The solution to the perturbation problem has a temporal dependence of the form $\exp(-\mathrm{i}\omega t) = \exp[-\mathrm{iRe}(\omega)t]\exp[\mathrm{Im}(\omega)t]$. Thus, the perturbations amplify (instability) when $\mathrm{Im}(\omega) > 0$ and damp out (stability) as long as $\mathrm{Im}(\omega) < 0$. For $\mathrm{Im}(\omega) = 0$, the perturbed field oscillates with neither amplifying nor damping. Therefore, in order to study the stability regime, we have to solve the SPH dispersion relation (46) in the short wavelength limit to get the dependence of the frequency on the local bandwidth factor, λ_a, and look for the sign of the imaginary part of ω.

6.1. Square cells

In the case where the particles are initially distributed on a grid of square cells, as in Fig. 1(a), all summations in Eqs. (34)–(38) vanish, with the exception of C_x and C_y. It then follows from the definitions in Eq. (45) that the only non-vanishing coefficients are γ_{xx} and γ_{yy}, and so the dispersion relation (46) reduces to a simple quadratic polynomial in ω^2:

$$\omega^4 - (\gamma_{xx}+\gamma_{yy})\omega^2 + \gamma_{xx}\gamma_{yy} = 0, \tag{53}$$

which admits the trivial solutions

$$\omega_+^2 = \gamma_{xx} = \frac{2p_0}{\rho_0}C_x, \qquad \omega_-^2 = \gamma_{yy} = \frac{2p_0}{\rho_0}C_y. \tag{54}$$

In this case, there is no contribution of the viscosity to the dispersion relation, because all the α's in Eq. (45) vanish identically. In terms of the bandwidth factor, λ_a, these solutions become

$$\begin{aligned}\omega_+^2\Delta s^2 &= -\frac{30p_0}{\pi\rho_0\lambda_a^4}\left[3 - \frac{(2+3\sqrt{2})}{\lambda_a} + \frac{11}{4\lambda_a^2}\right],\\ \omega_-^2\Delta s^2 &= -\frac{30p_0}{\pi\rho_0\lambda_a^4}\left[3 - \frac{(1+3\sqrt{2})}{\lambda_a} + \frac{9}{4\lambda_a^2}\right],\end{aligned} \tag{55}$$

for $h_0 = 2\Delta s$. The corresponding forms for $D = 3$, 4, and 5 are given in Appendix A.

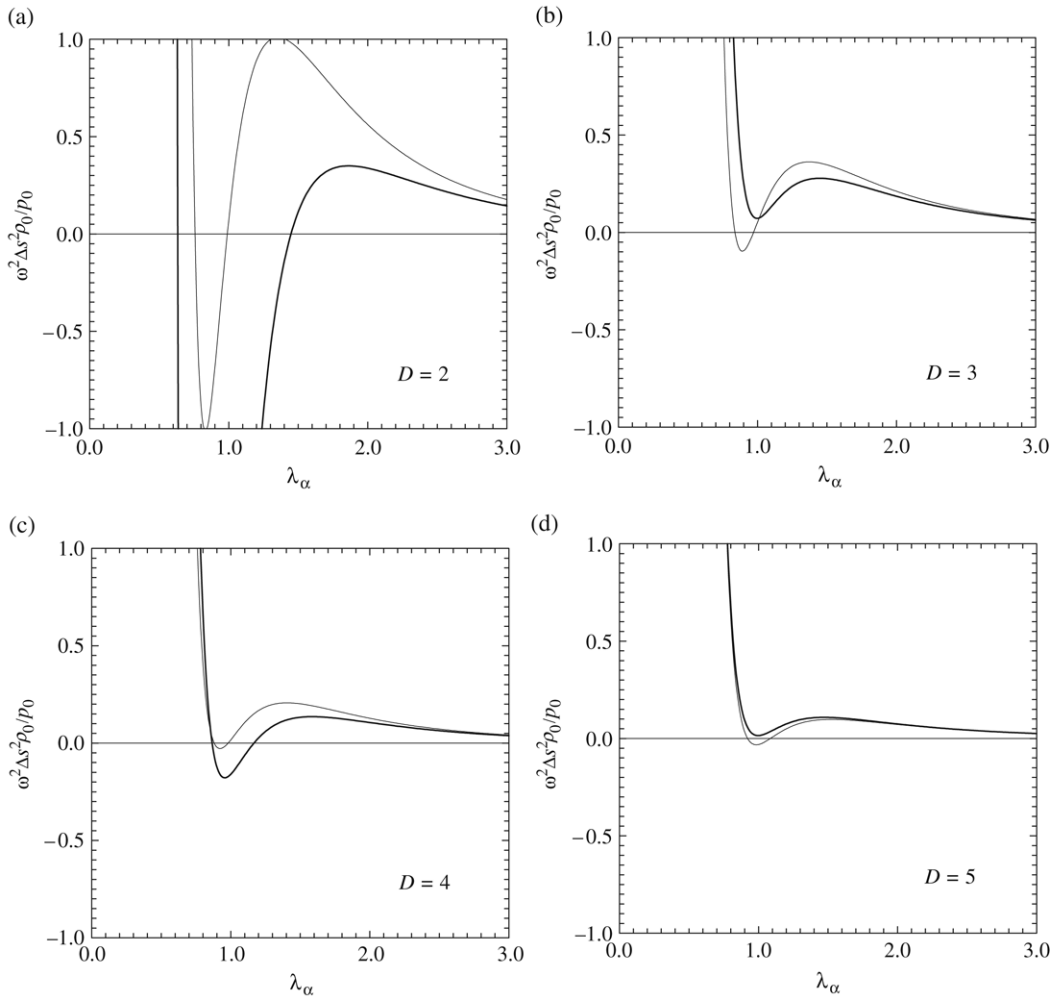

Fig. 2. Frequency as a function of the bandwidth factor, λ_a, for various sizes of the kernel support: (a) $D = 2$, (b) $D = 3$, (c) $D = 4$, and (d) $D = 5$, for the case in which the particles are initially distributed in a square cell grid. In each plot, the curve drawn with the thicker line corresponds to ω_+^2, while that drawn with the thinner line corresponds to ω_-^2.

We apply the present analysis to SPH simulations of the formation and dynamics of a stable circular liquid drop (see Section 7). Similar models of drop formation have been calculated by Nugent and Posch [4] and Meleán et al. [7]. Here we adopt the same parameters employed in those previous calculations. That is, we take a square array of equal mass ($m_a = m = 1$) particles, as shown in Fig. 1(a). We assume reduced units and take the van der Waals parameters to be $\bar{k}_B = 1$, $\bar{a} = 2$, $\bar{b} = 0.5$, and $T_0 = 0.2$ (see Section 7). A particle separation of $\Delta s = 0.75$ is taken in each direction, yielding an initial mean density $\rho_0 \approx 1.78$. With these parameters, the unperturbed pressure is $p_0 \approx -3.12$.

Fig. 2 shows the relation between the wave frequency and the bandwidth factor for varied sizes of the kernel support. In each plot, the behavior of ω_+^2 is shown by the thicker line, while that of ω_-^2 is shown by the thinner line. Although only bandwidth factors in the interval $0 < \lambda_a \leq 1$ are of practical significance for the case of an initially uniform-density medium, the curves have been drawn up to $\lambda_a = 3$ to show the asymptotic behavior of the frequency at large λ_a. When $D = 2$, a total of $\mathcal{N}_s = 12$ neighbors contribute to the kernel summations. In this case, $\omega_+^2 < 0$ for bandwidth factors in the range between $\lambda_a \approx 0.63$ and ≈ 1.45 (Fig. 2(a)). Note that ω_-^2 is negative within a much shorter interval, between $\lambda_a \approx 0.76$ and ≈ 0.99. When this happens, the frequency is a pure imaginary number equal to $\pm i\sqrt{\omega}$. Since both solutions are possible, the wave modes may either amplify or dampen, depending on whether the sign is positive or negative, respectively. Outside the above intervals, ω^2 is always positive, and therefore $\mathrm{Im}(\omega) = 0$ so that the amplitude of the perturbations will neither grow nor decrease with time. For higher sizes of the kernel

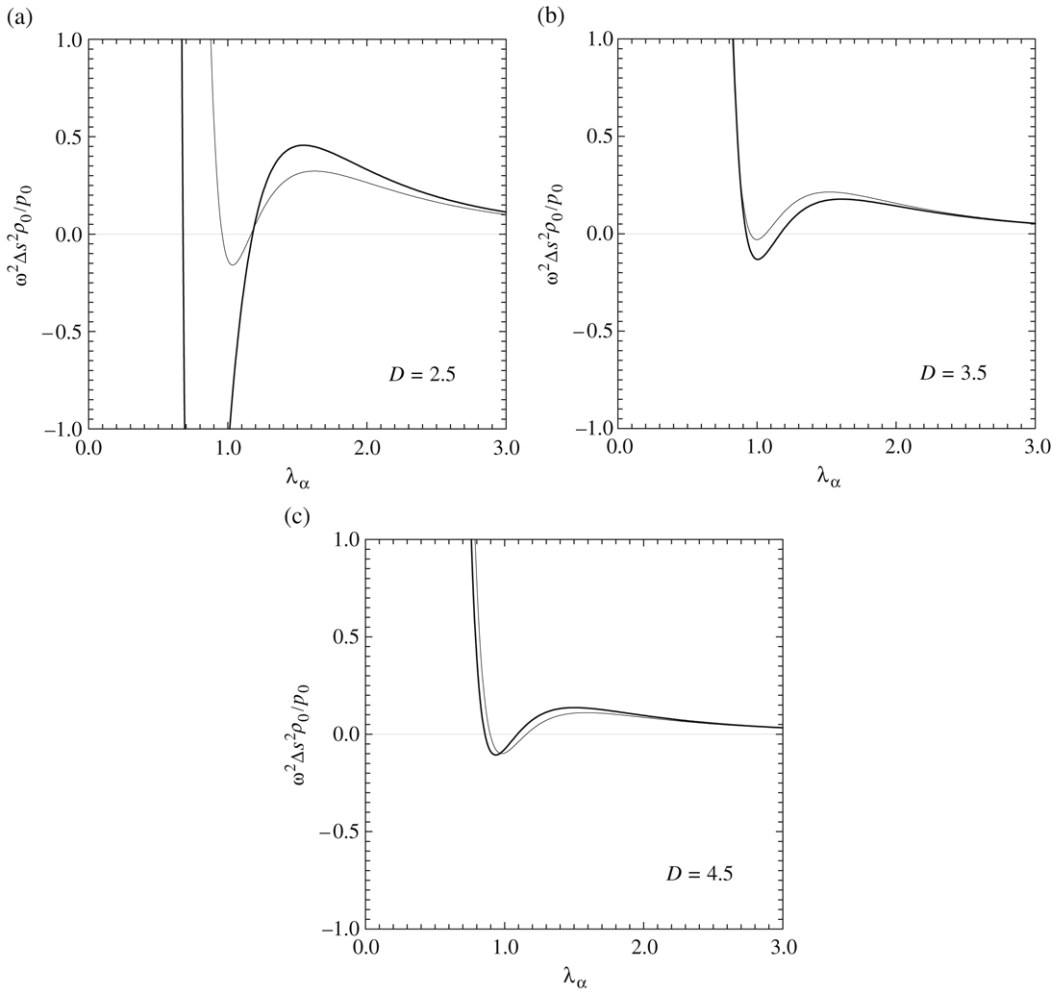

Fig. 3. Frequency as a function of the bandwidth factor, λ_a, for fractional sizes of the kernel support: (a) $D = 2.5$, (b) $D = 3.5$, and (c) $D = 4.5$, for the case in which the particles are initially distributed in a square cell grid. In each plot, the curve drawn with the thicker line corresponds to ω_+^2, while that drawn with the thinner line corresponds to ω_-^2.

support, the number of contributing neighbors increases (i.e., $\mathcal{N}_s = 28$ for $D = 3$, 48 for $D = 4$, and 80 for $D = 5$). In these cases, the intervals of λ_a for which the response may become unstable are considerably shorter compared to the case when $D = 2$, and so marginal stability occurs for most frequencies (Fig. 2(b)–(d)). This trend seems to be in good agreement with the results found by Belytschko and Xiao [14], that for Eulerian kernels with nodal integration, the range of instability decreases with increasing size of the kernel support. We see that for $D \geq 3$, unstable behavior may occur for small intervals around values of λ_a close to unity, that is, when the ADKE method essentially reduces to the fixed width kernel approach for which $h_a \approx h_0$. Thus, for particles distributed initially on a square cell grid, the ADKE method affects the behavior of standard SPH in the short wavelength limit, removing the tensile instability provided that the two involved parameters, namely β and ε in Eq. (15), are properly chosen. In Section 7, we describe numerical test simulations on the formation of circular liquid drops that validate this conclusion.

Fig. 3 depicts the dependence of the wave frequency with λ_a for $D = 2.5$ ($\mathcal{N}_s = 20$; Fig. 3(a)), 3.5 ($\mathcal{N}_s = 36$; Fig. 3(b)), and 4.5 ($\mathcal{N}_s = 68$; Fig. 3(c)). When $D = 2.5$, $\omega_+^2 < 0$ for bandwidth factors between $\lambda_a \approx 0.68$ and ≈ 1.18, while $\omega_-^2 < 0$ within $\lambda_a \approx 0.96$ and ≈ 1.17, meaning that when the dilation factor is increased from $D = 2$ to 2.5, the range of λ_a for which the solution may become tensile unstable is reduced. Thus, increasing the number of nearest neighbors not only broadens the region where the solution is marginally stable, but also affects quantitatively the behavior of ω_+^2 and ω_-^2. In particular, the solution for ω_-^2 shows a much less pronounced minimum. For larger

fractional values of D (=3.5 and 4.5), the curves are qualitatively similar to those obtained for integer values of $D \geq 3$. However, a close inspection of Figs. 2 and 3 shows that by gradually increasing the value of D, the minimum of ω_+^2 rises and eventually oscillates about $\omega^2 = 0$, becoming positive around $D = 3$ and 5. A similar oscillatory behavior is also seen for the minimum of ω_-^2, except that it always remains negative regardless of the value of D. Therefore, the details of the functional dependence of the frequency with λ_a are sensitive to the number of nearest neighbors allowed.

6.2. Face-centered cells

We shall now consider the form of the dispersion relation when the particles are distributed in a face-centered mesh, as shown in Fig. 1(b). As pointed out by Gray et al. [6], a transverse mode will cause adjacent lines of particles to move vertically relative to each other. In an SPH simulation of a gas or liquid, this results in the particles evolving from the initial square mesh array to one in which each vertical line is shifted up half a line. However, the final configuration would be the same, as if every second horizontal line would have been shifted by $\Delta s/2$. Again, this would correspond to a horizontally propagating mode with k_x equal to $\pi/\Delta s$ and k_y equal to zero.

In this case, the non-vanishing summations in Eq. (34) are: $A_{x,a}$, C_x, and C_y. Accordingly, also $A_{x,b}$ survives, and hence only the sum for F_{xx} in Eq. (35) will be non-zero. As a result, the dispersion relation (46) takes the form

$$\omega^4 - \mathrm{i}(\alpha_{xx} + \alpha_{yy})\omega^3 - (\gamma_{xx} + \gamma_{yy} + \alpha_{xx}\alpha_{yy})\omega^2 + \mathrm{i}(\alpha_{xx}\gamma_{yy} + \alpha_{yy}\gamma_{xx})\omega + \gamma_{xx}\gamma_{yy} = 0, \tag{56}$$

where

$$\alpha_{xx} = \frac{1}{\rho_0}(\eta + \zeta)F_{xx}, \qquad \alpha_{yy} = \frac{1}{\rho_0}\eta F_{xx},$$
$$\gamma_{xx} = 2\frac{p_0}{\rho_0}C_x + \left(c_0^2 - 2\frac{p_0}{\rho_0}\right)A_{x,a}^2, \qquad \gamma_{yy} = 2\frac{p_0}{\rho_0}C_y. \tag{57}$$

In contrast to the previous case, the contribution of viscosity appears as a consequence of the relative motion of the SPH particles when every second line is shifted along the x-direction. In the case when $h_0 = 2\Delta s$, each particle "a" has a total of 14 nearest neighbors, and so $A_{x,a}$, C_x, and C_y take the forms

$$A_{x,a} = \frac{15}{\pi\Delta s\lambda_a^4}\left[1 - \frac{(3\sqrt{13} - \sqrt{5})}{4\lambda_a} + \frac{17}{16\lambda_a^2}\right],$$
$$C_x = -\frac{15}{\pi\Delta s^2\lambda_a^4}\left[3 - \left(2 + \frac{3\sqrt{5}}{5} + \frac{11\sqrt{13}}{13}\right)\frac{1}{\lambda_a} + \frac{25}{8\lambda_a^2}\right], \tag{58}$$
$$C_y = -\frac{15}{\pi\Delta s^2\lambda_a^4}\left[3 - \frac{1}{2}\left(2 + \frac{9\sqrt{5}}{5} + \frac{17\sqrt{13}}{13}\right)\frac{1}{\lambda_a} + \frac{19}{8\lambda_a^2}\right],$$

while $F_{xx} = -\Delta s^2 A_{x,a}^2$. The corresponding expressions for $D = 3$, 4, and 5 are given in Appendix B.

Eq. (56) is solved numerically by means of a modified Newton–Raphson iteration scheme, using the same parameters as before. The coefficients of shear and bulk viscosity in reduced units are taken to be $\eta = 1$ and $\zeta = 0.1$, respectively. With this choice, the coefficients of Eq. (56) are strongly varying functions of λ_a, with variations of up 40 orders of magnitude in the interval $0 < \lambda_a \leq 1$. Therefore, arbitrary precision is required to get accurate results. For a typical calculation, the algebraic operations involved in the solution were carried out using 100 decimal figures. With this precision accuracy, the worst residues obtained were of the order of $\sim 10^{-60}$. The solution admits four independent complex roots, for the frequency as a function of λ_a. Figs. 4 and 5 show the imaginary part of these four frequencies in the interval $0 < \lambda_a \leq 1$ for various dilation factors. In each plot, the thickest line depicts the most interesting root for the purposes of our analysis. The other three frequencies always correspond to stable solutions, with negative $\mathrm{Im}(\omega)$ for most of the λ_a spectrum, except for large λ_a, where $\mathrm{Im}(\omega) \to 0$ asymptotically. When $D = 2$ ($\mathcal{N}_s = 14$; Fig. 4(a)), the response is marginally stable under tension [i.e., $\mathrm{Im}(\omega) \approx 0$] for $\lambda_a < 0.304$. For values of λ_a larger than this, $\mathrm{Im}(\omega) < 0$ and the wave amplitudes decay exponentially with time. A downward peak frequency occurs at $\lambda_a = 0.628$, where $\mathrm{Im}(\omega) \approx -20.52$. At $\lambda_a = 0.762$, $\mathrm{Im}(\omega)$ changes sign from negative to positive, and

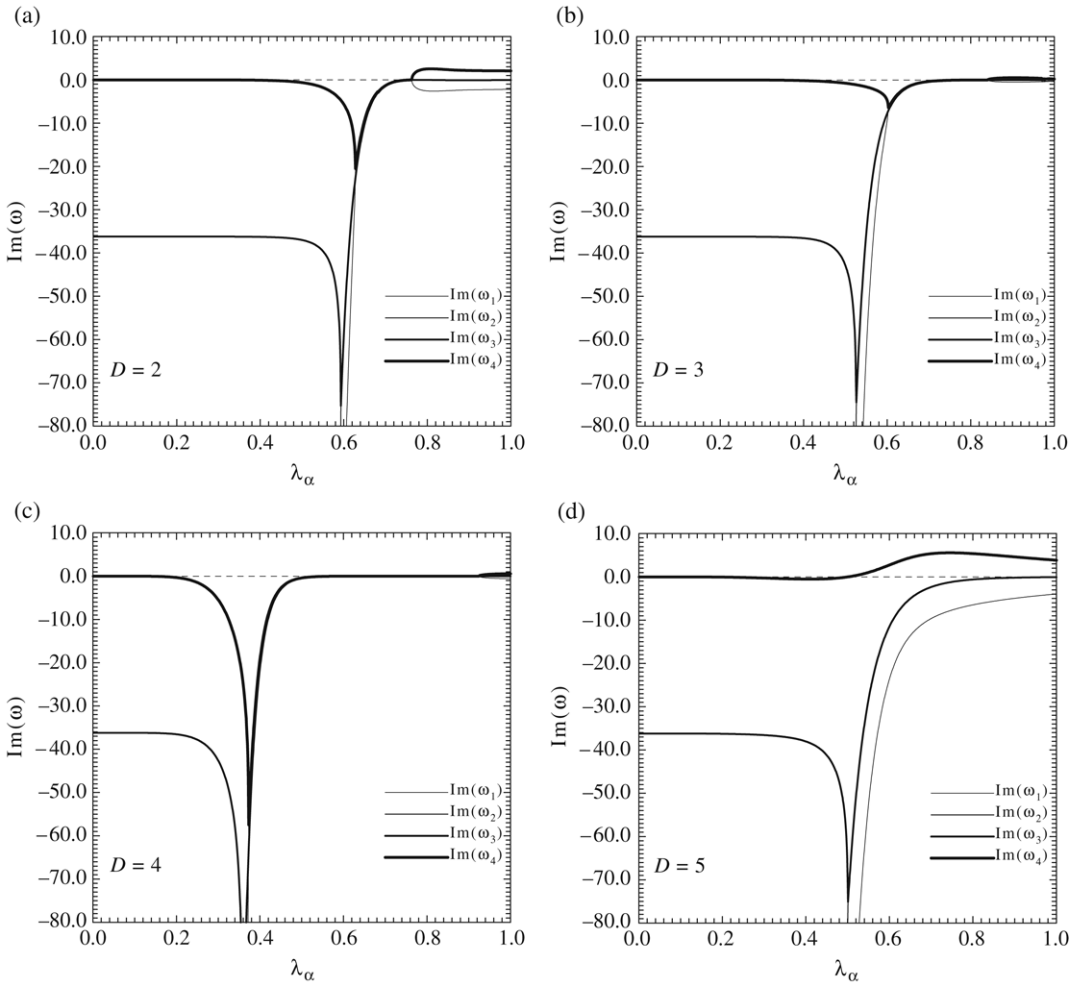

Fig. 4. Imaginary part of the frequency as a function of the bandwidth factor, λ_a, for various sizes of the kernel support: (a) $D = 2$, (b) $D = 3$, (c) $D = 4$, and (d) $D = 5$, for the case in which the particles are initially distributed in a face-centered lattice. All four roots of Eq. (56) are shown. The most significant frequency is ω_4 and corresponds to the thickest line.

the response becomes tensile unstable for larger λ_a. Note that beyond this threshold value, $\mathrm{Im}(\omega) \approx 0$ for two of the other roots (ω_2 and ω_3), while $\mathrm{Im}(\omega) < 0$ for ω_1 (thinnest line). For higher sizes of the kernel support, the behavior is qualitatively similar. In particular, when $D = 3$ ($\mathcal{N}_s = 28$; Fig. 4(b)), $\mathrm{Im}(\omega) \approx 0$ for $\lambda_a < 0.271$ (thickest line), and negative for larger λ_a. At $\lambda_a = 0.603$, a minimum, corresponding to $\mathrm{Im}(\omega) \approx -6.41$, is reached. The response becomes again marginally stable, with $\mathrm{Im}(\omega) \approx 0$, for $\lambda_a > 0.804$ and unstable, with $\mathrm{Im}(\omega) > 0$, for $\lambda_a \geq 0.841$. In contrast, the zone of marginal stability at low λ_a shortens considerably when $D = 4$ ($\mathcal{N}_s = 52$; Fig. 4(c)), while it broadens on the other side, with $\mathrm{Im}(\omega) \approx 0$ for $\lambda_a > 0.591$ and with $\mathrm{Im}(\omega)$ becoming positive at $\lambda_a = 0.925$. When $D = 5$ ($\mathcal{N}_s = 78$; Fig. 4(d)), the response is marginally stable for $\lambda_a < 0.138$ and stable for higher values up to $\lambda_a = 0.50$. For $\lambda_a > 0.50$, the response becomes unstable as $\mathrm{Im}(\omega) > 0$.

Fig. 5 depicts the dependence of the frequency with λ_a for fractional values of the dilation factor. The behavior for $D = 2.5$ ($\mathcal{N}_s = 20$; Fig. 5(a)), 3.5 ($\mathcal{N}_s = 36$; Fig. 5(b)), and 4.5 ($\mathcal{N}_s = 68$; Fig. 5(c)) is qualitatively similar to that in Fig. 4 for integer D. As before, the more significant root for the sake of the stability analysis is the one depicted with the thickest line, corresponding to ω_4. When we increase the size of the kernel from $D = 2$ to 2.5, the downward peak frequency becomes deeper and moves toward lower values of λ_a. The peak rises for $D = 3$ (Fig. 4(b)) and steeps again to much lower values for $D = 3.5$ (Fig. 5(b)). For this size, the frequency peaks at $\lambda_a \approx 0.22$ and then moves outward for larger sizes of the kernel. The strength of the peak fluctuates again between $D = 3.5$ and 4.5

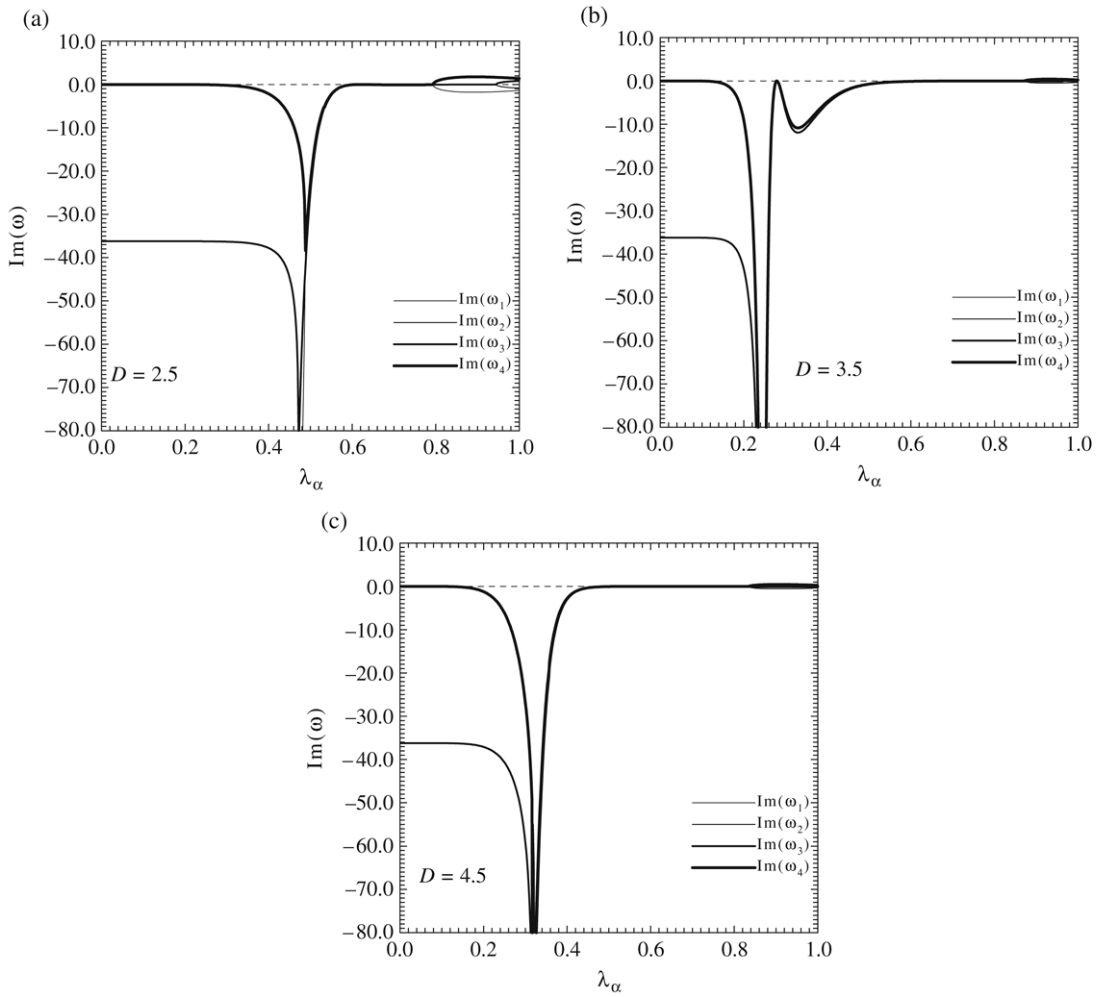

Fig. 5. Imaginary part of the frequency as a function of the bandwidth factor, λ_a, for fractional sizes of the kernel support: (a) $D = 2.5$, (b) $D = 3.5$, and (c) $D = 4.5$, for the case in which the particles are initially distributed in a face-centered lattice. All four roots of Eq. (56) are shown. The most significant frequency is ω_4 and corresponds to the thickest line.

(Fig. 5(c)), until it eventually dissipates for $D = 5$ (Fig. 4(d)). A direct inspection of the thickest curves in Figs. 4 and 5 clearly shows that wave damping is always faster for bandwidth factors between $\lambda_a \approx 0.2$ and ≈ 0.6, suggesting that a proper choice of the ADKE parameters must always point to values of λ_a that fall within this range. In general, $\mathrm{Im}(\omega_4)$ becomes positive toward large values of λ_a, i.e, for $\lambda_a \to 1$ when the ADKE method reduces to the fixed width kernel approach for which tensile instability is expected.

7. Numerical tests

The predictions of the above linear analysis may not exactly apply to highly nonlinear problems. In these cases, the tensile instability may even persist for values of the bandwidth factor for which the dispersion analysis predicts marginal or complete stability. However, because of the local (short wavelength) character of the SPH tensile instability, we expect the outcome of the numerical simulations to fit fairly well the predictions of the linear analysis. In this section, we first consider a series of numerical simulations of the formation of a van der Waals liquid drop in which the effects of viscosity and heat conduction are taken into account. In particular, this problem is a stringent test to validate the resolving power of the ADKE method in removing the tensile instability. Tests on more dynamical problems, including the nonlinear oscillations of a deformed liquid drop and the Sedov blast wave problem [18] are also presented.

7.1. Liquid drop model

We study the formation of a stable liquid drop at subcritical temperatures so that no evaporation of the fluid will take place during the whole evolution. Previous SPH calculations of this problem have shown that it is highly susceptible to unstable behavior under tension [4,7], and therefore it represents a very sensitive test to validate the effectiveness of the ADKE method in removing the tensile instability in simulations of a viscous fluid. For this test model, we assume a van der Waals fluid so that the constitutive relations are given by Eqs. (7) and (8). We choose reduced units and use the same parameters as employed in the linear dispersion analysis, namely $m = 1$, $\bar{a} = 2$, $\bar{b} = 0.5$, and $\bar{k}_{\rm B} = 1$. With these reduced units, the critical point of the van der Waals fluid occurs for $\rho_{\rm cr} = 2/3$, $p_{\rm cr} = 8/27$, and $T_{\rm cr} = 32/27$ [27]. In terms of the reduced variables $\rho \to \rho/\rho_{\rm cr}$, $p \to p/p_{\rm cr}$, and $T \to T/T_{\rm cr}$, Eq. (7) expresses the law of corresponding states. It will contain only the above reduced variables and not quantities pertaining to a particular liquid. Therefore, the reduced isotherms will be the same for all substances. The coefficients of thermal conductivity, shear, and bulk viscosity in reduced units are taken to be $\kappa = 5$, $\eta = 1$, and $\zeta = 0.1$, respectively. A value of κ this large serves to obtain a rapid temperature adjustment within the drop domain, implying that temperature fluctuations are effectively damped out. We recall that the results of the dispersion analysis (Figs. 2–5) apply to the limiting case of very large κ, and therefore they are valid in a medium which is free of temperature fluctuations. In addition, the outer medium is a vacuum, and so the drop is thermally insulated. That is, there is no heat flux between the drop and the vacuum, because there the thermal conductivity is exactly zero.

The simulations start with 900 SPH particles of equal mass ($m_a = m = 1$) placed on a Cartesian grid of square cells. Initially all particles are at rest with a separation distance $\Delta s = 0.75$ along the x- and y-axis. The initial density and temperature are such that they obey the constraints $\rho_0 < 1/\bar{b}$ and $\bar{k}_{\rm B} T_0 > 2\bar{a}\rho_0(1 - \rho_0\bar{b})^2$ for thermodynamic stability. Both these constraints are satisfied by assigning a temperature $T_0 = 0.2$ to each particle, and by determining the density from the summation interpolant (9) with the above particle separation. At a subcritical temperature of $T = 0.2$, an equilibrium circular drop with no external atmosphere is expected to form. In this way, no periodic boundary conditions are required far away from the initial square array of particles. Surface tension effects at the drop boundary are simulated by considering both the cohesive pressure, $-\bar{a}\rho^2$, in Eq. (7), and the cohesive energy, $-\bar{a}\rho$, in Eq. (8) separately from all other SPH terms. Following Nugent and Posch [4], this is done by evaluating the corresponding acceleration and heating summations with a fixed width kernel $W^H_{ab} = W(|\mathbf{x}_a - \mathbf{x}_b|, H)$, where $H \geq 2h_0$. This particular choice of the smoothing range is determined by stability considerations. In this way, the interaction range of the attractive cohesive forces is assumed to exceed that of all other smoothed forces appearing in the SPH equations of motion. A similar observation led to a substantial improvement of the interface stability properties with the continuum-surface-force method employed by Morris [28]. Because of the crippling deficiency of particles at the drop boundary, the density there will be lower than the uniform value carried by the interior particles, yielding a density distribution which is not discontinuous at the boundary. Although this may affect the dependence of the surface tension on temperature, it allows the drop surface evolution to proceed stably, without the use of any particular boundary condition. This is true because the cohesive forces largely cancel in the bulk of the drop, except for a small strip H around the drop surface, where the particles are accelerated in the direction of the inward surface normal. This translates into a net surface tension force whose effect is to smooth out regions of high curvature in an attempt to reduce the total surface area and hence the surface energy.

We consider four sequences of model calculations, all starting with a square cell grid and identical initial conditions. The reason for choosing this mesh is that it appears to be the most unstable according to our analysis and those of Gray et al. [6] and Swegle [29]. In addition, it allows comparison with previous calculations for this test case [4, 7]. Each sequence is defined by fixing the value of D and varying the ADKE parameters β and ε. In particular, we choose $D = 2$, 3, 4, and 5, and values of β and ε in the intervals [0.5, 1.0) and [0.5, 0.9], respectively. Since during a typical evolution the variations of the bulk density and temperature are small, the local bandwidth factors, λ_a, are mostly determined by the value of β rather than the value of ε. However, the pattern of particle positions in the final equilibrium drop is highly sensitive to ε.

At the beginning of a typical evolution, the work done by the pressure forces within the free surface induces an inward motion of the boundary particles. During this short initial phase, part of the surface tension energy is converted into internal liquid movement with a consequent sharp increase of the kinetic energy. For most of the models, complete drop circularization is approximately achieved during the first sixth of the evolution time. By the end of this period, more than 95% of the induced kinetic energy has been lost by viscous dissipation. In this process, the internal energy

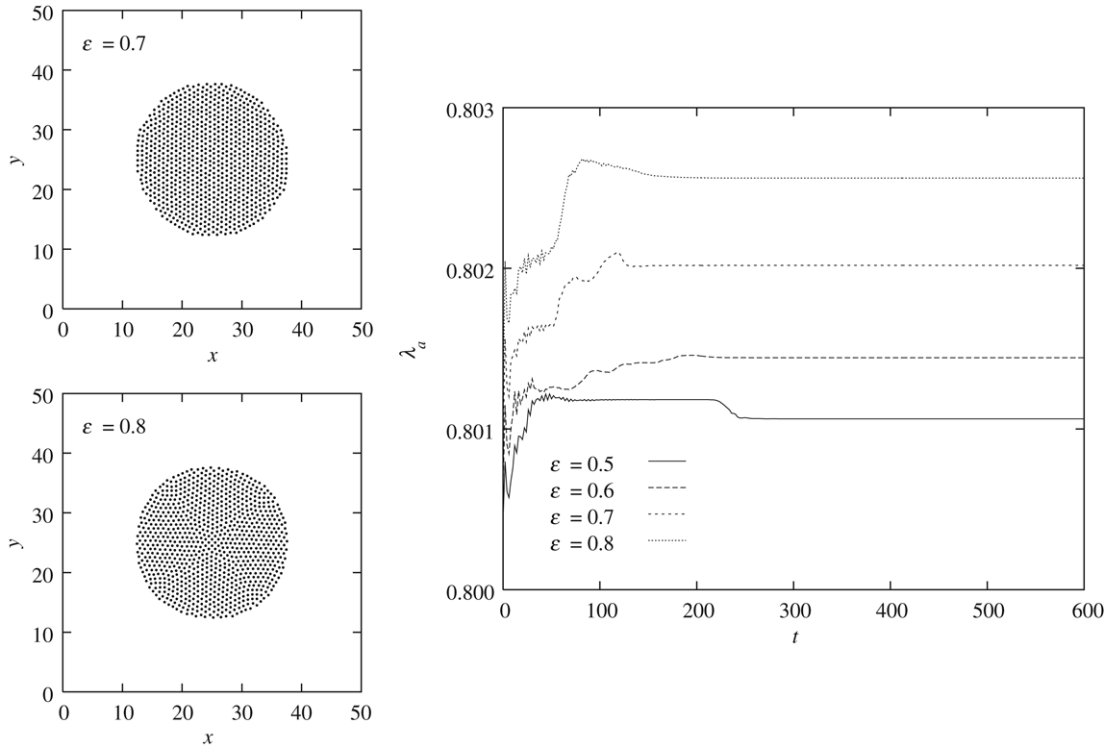

Fig. 6. Particle positions in the (x, y)-plane (top and bottom panels on the left) showing the structure of a circular liquid drop, with $D = 2$, $\beta = 0.8$, and varied ε. The right panel shows the variation with time of the average value of λ_a for the same drops. The variations for $\varepsilon = 0.5$ and 0.6 are also shown.

increases as a result of the excess heating produced by the internal friction near the free surface of the drop. Part of this heating is balanced by heat conduction, thus causing the rate of increase of the internal energy to slow down such that the total energy is conserved. The remainder of the evolution is characterized by a very slow dissipation of the internal liquid movement, accompanied by an equally slow increase of the thermal energy. The calculations are terminated when the drop is sufficiently close to thermo-mechanical equilibrium, i.e., when the kinetic energy tends to almost zero and the thermal energy ceases to increase. With a constant timestep size of $\Delta t = 0.005$, a typical equilibrium drop is formed after about 120,000 computational cycles.

The sequence of models with $D = 2$ has always resulted in stable calculations, regardless of the value of λ_a. However, this is not in contradiction with the results of Fig. 2(a), because the range of λ_a for which $\omega^2 < 0$ may also imply solutions with $\mathrm{Im}(\omega) < 0$, and hence suppression of the tensile instability. The top and bottom panels on the left of Fig. 6 show the final equilibrium drops for $\beta = 0.8$, when $\varepsilon = 0.7$ and 0.8, respectively. Similar stable patterns were found for all other values of β and ε. The right panel depicts the time variation of the average value of λ_a for these two calculations. The curves for $\varepsilon = 0.5$ and 0.6 are also shown. We see that no signs of the tensile instability are apparent from the positions of the SPH particles. For $\varepsilon = 0.7$, the particles are ordered in a face-centered manner, while a different particle distribution is obtained when $\varepsilon = 0.8$, implying that the final equilibrium pattern is sensitive to variations of ε.

For $D = 3$, all calculations with $0.5 \leq \beta \leq 0.7$ and varied ε, corresponding to values of λ_a between $\approx$0.5 and $\approx$0.7, produced stable results in good agreement with the predictions of Fig. 2(b), which indicate marginal stability. Only when $\beta = 0.8$, do the particles clump together in pairs, as shown in Fig. 7. In this case, $\lambda_a \approx 0.8$, which is close to the lower end of the interval where $\omega_-^2 < 0$ in Fig. 2(b). We note that for $\varepsilon = 0.5$, pairwise clumping occurs only toward the drop center, while for higher ε, the instability spreads over a progressively larger region until it involves the entire drop when $\varepsilon = 0.8$. By comparison, Fig. 8 depicts the equilibrium drops for $\beta = 0.9$. In this case, the corresponding values of λ_a are well inside the range where $\omega_-^2 < 0$. However, we may see that the particle positions roughly preserve their initial square cell arrangement, implying that no tensile instability is present. The solution for

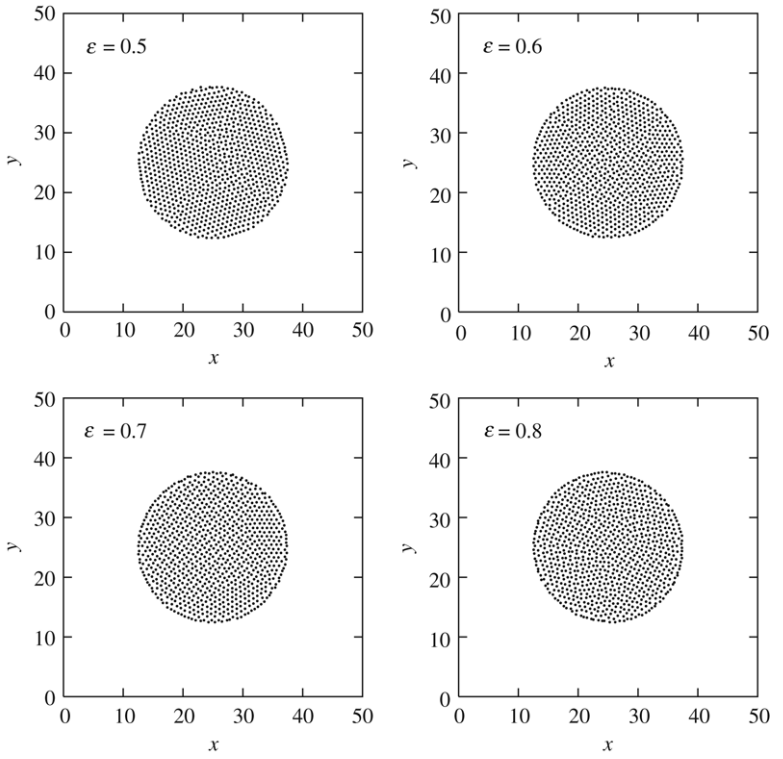

Fig. 7. Particle positions in the (x, y)-plane showing the structure of a circular liquid drop, with $D = 3$, $\beta = 0.8$, and varied ε.

this choice of β may well correspond either to wave damping as a result of having $\mathrm{Im}(\omega_-) < 0$ or marginal stability as implied by the other solution (thicker line in Fig. 2(b)), where $\omega_+^2 > 0$ for all values of λ_a.

When the dilation factor is raised to $D = 4$, the numerical results also fit the predictions for the dispersion relation. In particular, the four panels of Fig. 9 show the equilibrium drops produced for $\varepsilon = 0.8$ and varied β. The top panels display the particle positions when $\beta = 0.6$ and 0.7. For these two models, the corresponding bandwidth factors always fall in the region where both ω_+^2 and ω_-^2 are positive (Fig. 2(b)), and therefore no signs of instability are evident in the structure of the equilibrium drops. In contrast, a well-marked clumping of particles in pairs is visible in most of the drop domain when $\beta = 0.8$ (bottom left panel). This is expected because for $\beta = 0.8$, the values of λ_a are close enough to the left extreme of the interval where both ω_+^2 and ω_-^2 become negative in Fig. 2(c). The tensile instability is also evident in the bottom right panel, corresponding to $\beta = 0.92$, for which the values of λ_a are now well inside the region of instability in Fig. 2(c). Pairwise clumping is again evident in the bulk of the drop, while toward its surface the particles appear to be clustered into a concentric ring.

The clustering of particles into a well-defined pattern consisting of alternating concentric dense rings and voids in the final drop structure is the result of the tensile instability when standard SPH is used, coupled to moderately high sizes of the kernel support [4,7]. Since the liquid drop remains essentially homogeneous during the evolution, a direct inspection of Eq. (15) shows that for $\varepsilon \to 1$ and $\beta \to 1$, $\lambda_a \to 1$, and so the ADKE method reduces to the usual kernel approach with fixed width. This is confirmed by the results shown in Fig. 10, which depict the final SPH particle positions when $D = 5$, and ($\varepsilon = 0.5$, $\beta = 0.5$; left panel) and ($\varepsilon = 0.8$, $\beta = 0.96$; right panel). The tensile instability is suppressed in the left panel, as expected from the results of our linear analysis (see Fig. 2(d)). Conversely, when $\beta \to 1$ the instability appears in the form of clustering into concentric rings. Similar structures were obtained for all models with $\beta \geq 0.8$, regardless of the value of ε. Note that for these latter models, the local bandwidth factors fall either sufficiently close to or well inside the range where $\omega_-^2 < 0$, according to Fig. 2(d).

Finally, a few calculations were tried with the particles placed initially on a face-centered grid, as shown in Fig. 1(b). The results from these models are useful to compare with the linear stability predictions of Fig. 4. For face-centered arrays with $D \leq 4$, the numerical results fit very well the expected behavior given by the thickest curves

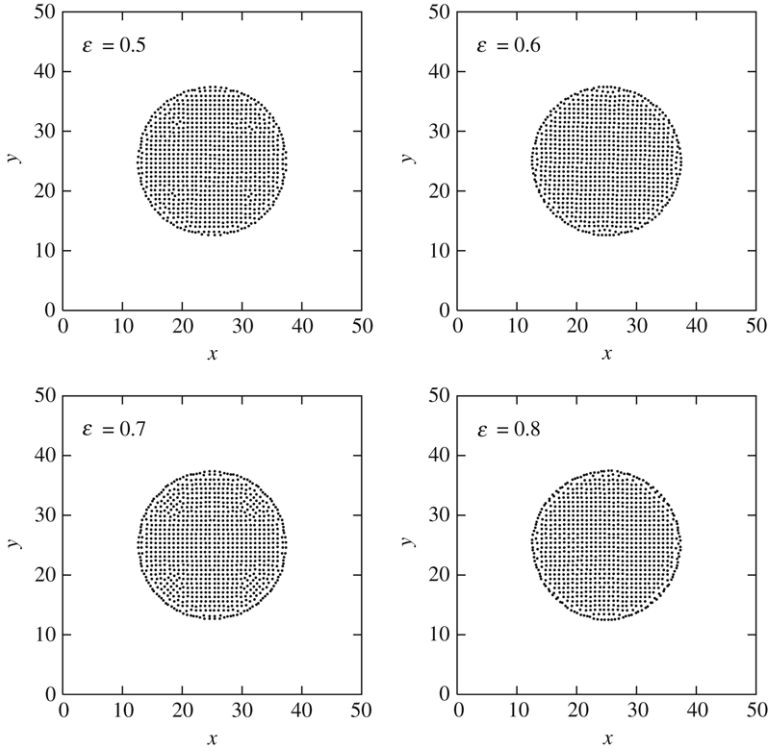

Fig. 8. Same of Fig. 7 but with $\beta = 0.9$.

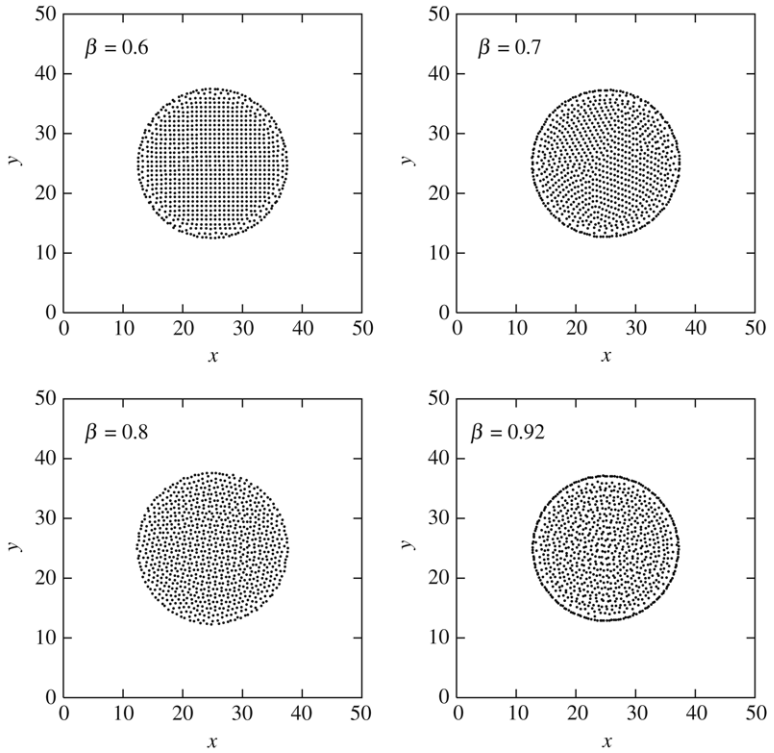

Fig. 9. Particle positions in the (x, y)-plane showing the structure of a circular liquid drop, with $D = 4$, $\varepsilon = 0.8$, and varied β.

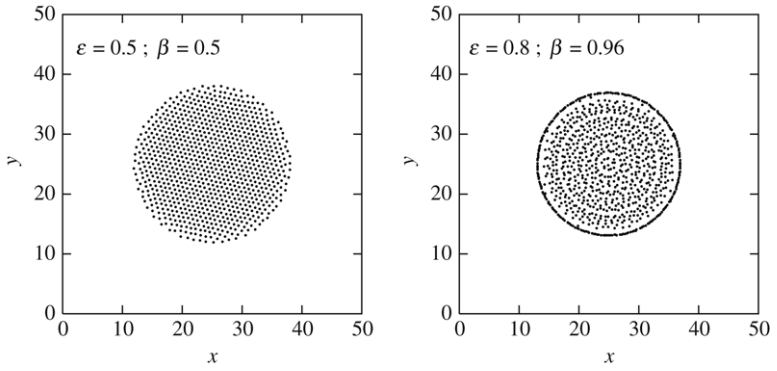

Fig. 10. Particle positions in the (x, y)-plane showing the structure of a circular liquid drop, with $D = 5$. The left panel displays the result for $\varepsilon = 0.5$ and $\beta = 0.5$, while the right panel shows the final configuration obtained with $\varepsilon = 0.8$ and $\beta = 0.96$.

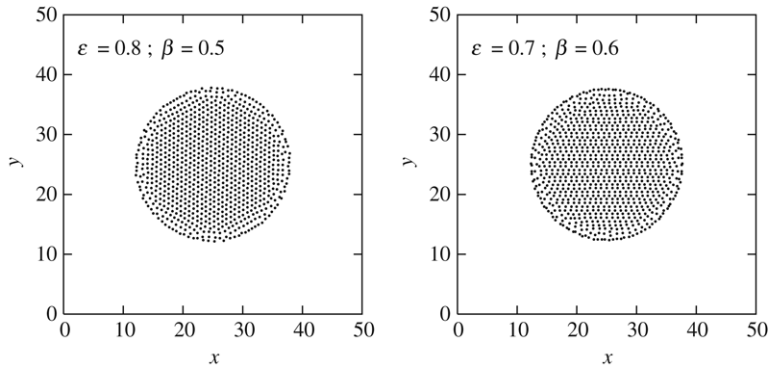

Fig. 11. Particle positions in the (x, y)-plane showing the structure of a circular liquid drop, with $D = 5$. In contrast to the previous plots, the particles were initially placed on a face-centered grid. The left panel shows the final drop configuration for $\varepsilon = 0.8$ and $\beta = 0.5$, while the right panel shows the result for $\varepsilon = 0.7$ and $\beta = 0.6$.

in Fig. 4(a)–(c). The results for two model calculations with $D = 5$ are shown in Fig. 11. The right panel in this figure corresponds to the case when $\varepsilon = 0.7$ and $\beta = 0.6$. A pairwise instability is clearly evident from the distribution of the particles. With this choice of the ADKE parameters, λ_a takes values around ≈ 0.6, for which $\mathrm{Im}(\omega_4) > 0$ according to Fig. 4(d). In addition, the left panel (with $\varepsilon = 0.8$ and $\beta = 0.5$) shows a perfectly stable configuration where the initial face-centered array is essentially preserved. For this particular model, λ_a oscillates about ≈ 0.5, which approximately marks the point where $\mathrm{Im}(\omega_4)$ changes sign from negative (stable) to positive (unstable), according to Fig. 4(d). Further test calculations with $D = 5$ and $\lambda_a > 0.6$ also confirm the predictions of Fig. 4(d) for unstable behavior.

7.2. *Oscillating viscous drop*

As a further test model, we consider the large-amplitude oscillations of a liquid drop that is released from a static elliptic shape, resulting from deforming an equilibrium circular drop of radius R. The unperturbed drop corresponds to the stable drop shown in the upper right panel of Fig. 8, with $D = 3$ and ADKE parameters $\beta = 0.9$ and $\varepsilon = 0.6$. An elliptic shape with aspect ratio $a/b = 4$ is obtained by means of the area-preserving coordinate transformation

$$x' = (1 + s)^{-1} x,$$
$$y' = (1 + s) y,$$

where s denotes the elongation, and the semimajor and semiminor axes are defined by the relations $a = (1 + s)R$ and $b = R/(1 + s)$, respectively. The above transformation converts the circle into an ellipse with the major axis aligned with the y-axis, as shown in the first panel of Fig. 12. The successive panels in this figure display the resolved

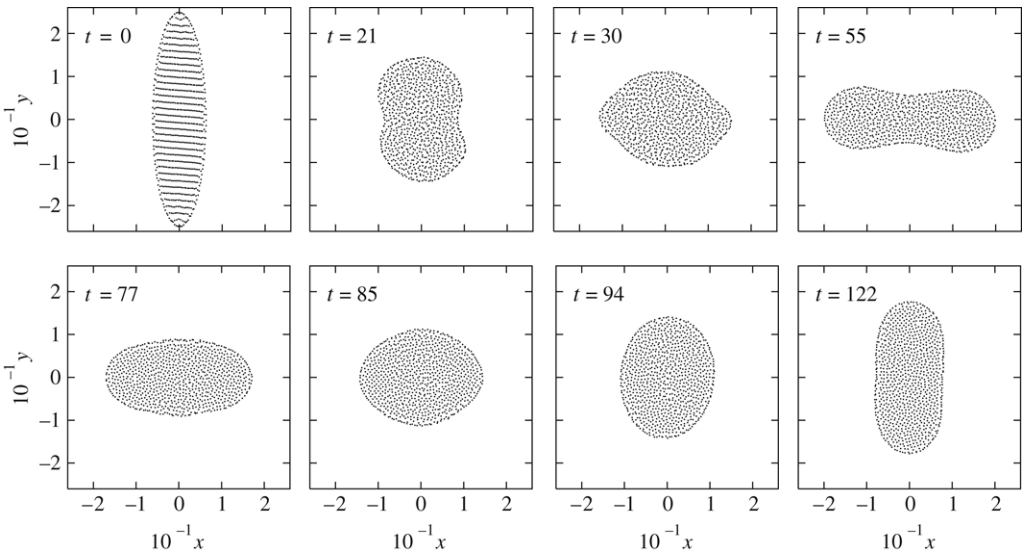

Fig. 12. Sequence of times showing the first period of oscillation of a liquid drop when it is released from an elliptic shape with aspect ratio $a/b = 4$ ($t = 0$). In all panels, the time is given in reduced units.

evolution of the drop during its first period of oscillation. The evolution time is given in reduced units. When the drop is released from its elongated shape, it contracts along its major axis ($t = 21$), because most of its surface energy is transformed into internal liquid movement. As a result, a counterflow develops, which soon transforms into a nearly steady drifting motion, which then conveys the drop through a transient nearly circular shape ($t = 30$) before reaching a point of maximum elongation along the x-axis ($t = 55$). At this time, most of the undamped internal kinetic energy is converted into surface energy. Soon after, the drop contracts under surface tension along the x-axis as the rim pressure exceeds the stagnation pressure inside it. During its contraction, the drop passes again through an approximate circular shape before setting into a prolate shape toward completion of the first oscillation period ($t = 122$). This oscillatory behavior will continue in time until the drop loses its internal kinetic energy by viscous dissipation and returns to its equilibrium circular shape.

We may see from the sequence of Fig. 12 that the particles within the oscillating drop are distributed irregularly, due to the internal motion. The distribution is such that no signs of clumping are evident, implying that the calculation is free of the effects of the tensile instability. Further test calculations for this drop model with $0.5 \leq \varepsilon \leq 0.8$ and $\beta = 0.9$ have produced almost identical transient shapes with no symptoms of the tensile instability being apparent from the positions of the SPH particles. Deformed drops with lower initial prolate aspect ratios ($a/b = 2$ and 3) and ADKE parameters $\beta = 0.9$ and $\varepsilon = 0.6$ also evolved into transient irregular particle distributions without evidence for clustering or clumping.

7.3. The Sedov blast wave

As a third test, we consider the Sedov point explosion problem in cylindrical geometry. This problem involves the self-similar propagation of a blast wave from a spiky pressure perturbation in a homogeneous medium at rest. Sedov [18] derived the analytical solution for this problem by assuming that the external pressure is negligible compared to that inside the explosion. The point explosion is assumed to occur at the origin ($r = 0$) at time $t = 0$. We consider a gas of uniform density $\rho_i = 1$, adiabatic index $\gamma = 1.4$, and pressure $p_i = 1.0 \times 10^{-5}$, except for a small area of radius $r_0 = 0.025$ about the origin, where the pressure is given by

$$p_0 = \frac{(\gamma - 1)e}{\pi r_0^2},$$

with e denoting the specific internal energy. This initial parameters are the same employed by Omang et al. [30]. To the right of the expanding shock, the density, velocity, and pressure at any time are given by $\rho_R(r, t) = \rho_i$, $v_R(r, t) = 0$, and $p_R(r, t) = p_i$, respectively.

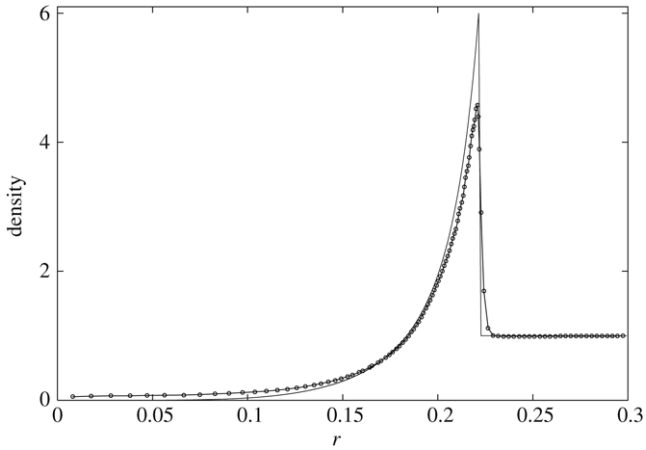

Fig. 13. Averaged radial density profile over the azimuthal angle for the two-dimensional Sedov cylindrical point explosion at $t = 0.05$. The numerical solution (dotted line) was obtained with 61,050 SPH particles and ADKE parameters $\beta = 0.9$ and $\varepsilon = 0.6$. The analytical profile (solid line) is shown for comparison.

We use the (r, ϕ)-plane to represent the flow. The computational domain consists of a circular area of radius $R = 0.3$ filled with n concentric circles, each consisting of $N_j = 10j$ particles, with $j = 1, 2, \ldots, n$. The radial separation between consecutive circles is $\Delta r = R/n$, and the angular interparticle separation is $\Delta\phi_j = \pi/(5j)$. With this choice, the mass of all particles belonging to the jth circle is $m_j = (2j - 1)m_1/j$ for $j \geq 2$, where $m_1 = \pi(\Delta r)^2\rho_i/10$ is the mass of a particle pertaining to the first circle ($j = 1$). The ADKE parameters for this test case were chosen to be $\beta = 0.9$ and $\varepsilon = 0.6$, as for the oscillating drop of previous section. The model starts with $h_0 = 2\Delta r$ and 61,050 particles, corresponding to $n = 110$ concentric circles. The timestep was fixed to $\Delta t = 5.0 \times 10^{-5}$.

The resulting radial density profile at $t = 0.05$ after the explosion is shown in Fig. 13. The solid line depicts the exact solution, and the dotted one the numerically obtained result. The strong jump in the density as well as the shock position are fairly well reproduced. A similar solution was previously found by Sigalotti et al. [21] using slightly different ADKE parameters. Compared to Omang et al. [30], the density jump in Fig. 13 is considerably sharper. The calculation converges to a peak shock density of $\approx$4.6 (exact value 6), which is similar to the value reported by Shashkov and Wendroff [31] using different grid refinements with their composite Lagrangian code. Fig. 14 displays a kernel plot at $t = 0.05$, where about a quarter of the total number of particles is shown for the sake of clarity. The round shape of the outgoing shock is also well reproduced and the adaptive nature of the ADKE procedure is evident as the area of the kernels progressively reduce toward the location of the shock front, where it becomes the smallest. The azimuthal symmetry of the expansion is also very well preserved. While this test problem is not indicative of the tensile instability, it is useful to illustrate the adaptive character of the ADKE method.

8. Conclusions

In this work, we have demonstrated that when the standard SPH method is made to rely on an adaptive density kernel estimation (ADKE) procedure like the one proposed by Silverman [17], the tensile instability can be completely removed in calculations of a viscous fluid with a van der Waals equation of state. In principle, the method should also be applicable to elastic solids and other fluids with stiff equations of state. In brief, the ADKE method consists of constructing a collection of local bandwidth factors, or kernel estimates, evaluated at the position of particles, such that the width of the kernel interpolant is allowed to vary from point to point. The method combines intrinsic features of both the kernel and the nearest neighbor approaches in such a way that the minimum necessary smoothing is effectively applied to the data. This aspect improves both the accuracy and stability of standard SPH. The ADKE algorithm is simple to implement, and does not require special modifications when applied to three-dimensional problems.

We first analyzed the method by linearly perturbing the SPH equations for a heat-conducting, viscous fluid with small oscillations. The resulting dispersion relation was solved in the limit for short wavelengths to yield the wave

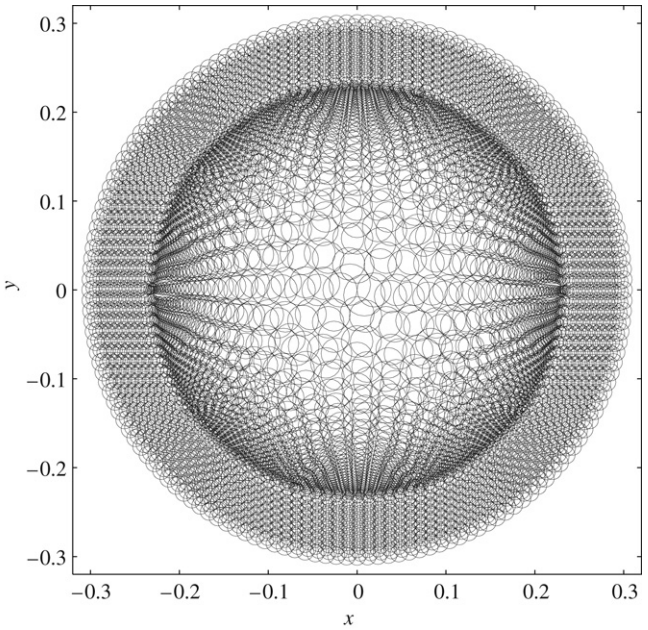

Fig. 14. Kernel plot for the same Sedov explosion of Fig. 13 at $t = 0.05$, showing the adaptive character of the ADKE procedure. For clarity, only a quarter of the total number of particles is depicted. As expected, the smallest kernels occur on the outgoing shock front.

frequency as a function of the bandwidth factors. Application of the stability analysis for varied sizes of the kernel support and varied initial distributions of the particles shows that the tensile instability can be reduced, or even, suppressed for a wide range of the free parameters involved in the definition of the bandwidth factors. Numerical SPH simulations with the ADKE method confirm the analytical results for the dispersion relation. In particular, we study the formation of a circular liquid drop at a subcritical temperature so that no evaporation of the liquid will take place during the evolution. Since this test problem is highly susceptible to unstable behavior in the tensile regime, it represents a valuable test case to confirm the validity of the linear dispersion analysis. Compared with the artificial-repulsive-force method of Monaghan [5] and Gray et al., [6], the ADKE method seems to do a superior job in removing the tensile instability, and also produces a much better description of the free surface, as we may further see by comparing it with the drop calculations of Meleán et al. [7], which rely on adding an artificial stress to the SPH equation of motion in the way suggested by the method of Gray et al. [6]. Tests on more dynamical problems, including the nonlinear oscillations of a highly deformed drop and the Sedov blast wave, confirm the resolving power of the ADKE method.

Acknowledgements

We thank the anonymous referee for having provided a number of comments and suggestions that have greatly improved this paper. This work is financially supported by the Instituto Venezolano de Investigaciones Científicas (IVIC). We also acknowledge the Fondo Nacional de Ciencia, Tecnología e Innovación (Fonacit) of Venezuela for partial support.

Appendix A. Square cells: Roots of the dispersion relation for varied integer sizes of the kernel support

In this appendix, we write down the roots of the dispersion equation (53), as defined by Eq. (54), for varied integer sizes of the kernel support. The roots are expressed in terms of the bandwidth factor λ_a. In particular, we find that

$$\omega_+^2 \Delta s^2 = -\frac{160 p_0}{27\pi\rho_0\lambda_a^4}\left[6 - \frac{2}{3}\left(8 + 3\sqrt{2} + \frac{12\sqrt{5}}{5}\right)\frac{1}{\lambda_a} + \frac{52}{9\lambda_a^2}\right],$$
$$\omega_-^2 \Delta s^2 = -\frac{160 p_0}{27\pi\rho_0\lambda_a^4}\left[6 - \frac{2}{3}\left(4 + 3\sqrt{2} + \frac{18\sqrt{5}}{5}\right)\frac{1}{\lambda_a} + \frac{44}{9\lambda_a^2}\right], \tag{A.1}$$

for $h_0 = 3\Delta s$;

$$\omega_+^2\Delta s^2 = -\frac{15p_0}{4\pi\rho_0\lambda_a^4}\left[6-\frac{1}{4}\left(8+3\sqrt{2}+\frac{12\sqrt{5}}{5}+6\sqrt{10}+\frac{44\sqrt{13}}{13}\right)\frac{1}{\lambda_a}+\frac{97}{16\lambda_a^2}\right],$$
$$\omega_-^2\Delta s^2 = -\frac{15p_0}{4\pi\rho_0\lambda_a^4}\left[6-\frac{1}{4}\left(4+3\sqrt{2}+\frac{18\sqrt{5}}{5}+6\sqrt{10}+\frac{34\sqrt{13}}{13}\right)\frac{1}{\lambda_a}+\frac{83}{16\lambda_a^2}\right], \tag{A.2}$$

for $h_0 = 4\Delta s$; and

$$\begin{aligned}\omega_+^2\Delta s^2 &= -\frac{192p_0}{125\pi\rho_0\lambda_a^4}\left[\frac{19}{2}-\frac{1}{5}\left(\frac{158}{5}+3\sqrt{2}+\frac{12\sqrt{5}}{5}+6\sqrt{10}\right.\right.\\ &\quad\left.\left.+\frac{44\sqrt{13}}{13}+\frac{36\sqrt{17}}{17}+3\sqrt{18}\right)\frac{1}{\lambda_a}+\frac{93}{10\lambda_a^2}\right],\\ \omega_-^2\Delta s^2 &= -\frac{192p_0}{125\pi\rho_0\lambda_a^4}\left[\frac{19}{2}-\frac{1}{5}\left(\frac{127}{5}+3\sqrt{2}+\frac{18\sqrt{5}}{5}+6\sqrt{10}\right.\right.\\ &\quad\left.\left.+\frac{34\sqrt{13}}{13}+\frac{68\sqrt{17}}{17}+3\sqrt{18}\right)\frac{1}{\lambda_a}+\frac{19}{2\lambda_a^2}\right],\end{aligned} \tag{A.3}$$

for $h_0 = 5\Delta s$.

Appendix B. Face-centered cells: Expressions for $A_{x,a}$, C_x, and C_y for varied integer sizes of the kernel support

The functional dependences of $A_{x,a}$, C_x, and C_y on the bandwidth factor, λ_a, for a face-centered grid are:

$$A_{x,a} = -\frac{40}{27\pi\Delta s\lambda_a^4}\left[3-\frac{(\sqrt{5}-3\sqrt{13}+5\sqrt{29})}{3\lambda_a}+\frac{37}{12\lambda_a^2}\right],$$
$$C_x = -\frac{40}{27\pi\Delta s^2\lambda_a^4}\left[7-\frac{2}{3}\left(8+3\sqrt{5}+\frac{11\sqrt{13}}{13}+\frac{27\sqrt{29}}{29}\right)\frac{1}{\lambda_a}+\frac{293}{36\lambda_a^2}\right], \tag{B.1}$$
$$C_y = -\frac{40}{27\pi\Delta s^2\lambda_a^4}\left[7-\frac{1}{3}\left(8+9\sqrt{5}+\frac{17\sqrt{13}}{13}+\frac{33\sqrt{29}}{29}\right)\frac{1}{\lambda_a}+\frac{215}{36\lambda_a^2}\right],$$

for $h_0 = 3\Delta s$;

$$A_{x,a} = \frac{15}{32\pi\Delta s\lambda_a^4}\left[1-\frac{1}{4}\left(3\sqrt{13}-\sqrt{5}-5\sqrt{29}-\sqrt{37}+3\sqrt{45}+7\sqrt{53}-5\sqrt{61}\right)\frac{1}{\lambda_a}+\frac{53}{64\lambda_a^2}\right],$$
$$\begin{aligned}C_x &= -\frac{15}{16\pi\Delta s^2\lambda_a^4}\left[13-\frac{1}{2}\left(8+3\sqrt{5}+\frac{55\sqrt{13}}{13}\right.\right.\\ &\quad\left.\left.+\frac{27\sqrt{29}}{29}+\frac{19\sqrt{37}}{37}+\frac{27\sqrt{45}}{45}+\frac{51\sqrt{53}}{53}+\frac{43\sqrt{61}}{61}\right)\frac{1}{\lambda_a}+\frac{905}{64\lambda_a^2}\right],\\ C_y &= -\frac{15}{16\pi\Delta s^2\lambda_a^4}\left[13-\frac{1}{4}\left(8+9\sqrt{5}+\frac{85\sqrt{13}}{13}+\frac{33\sqrt{29}}{29}+\frac{73\sqrt{37}}{37}\right.\right.\\ &\quad\left.\left.+\frac{81\sqrt{45}}{45}+\frac{57\sqrt{53}}{53}+\frac{97\sqrt{61}}{61}\right)\frac{1}{\lambda_a}+\frac{803}{64\lambda_a^2}\right],\end{aligned} \tag{B.2}$$

for $h_0 = 4\Delta s$; and

$$
\begin{aligned}
A_{x,a} &= -\frac{24}{125\pi\,\Delta s\lambda_a^4}\left[1-\frac{1}{5}\left(\sqrt{5}-3\sqrt{13}+5\sqrt{29}+\sqrt{37}-3\sqrt{45}-7\sqrt{53}+5\sqrt{61}-2\sqrt{85}\right)\frac{1}{\lambda_a}\right.\\
&\quad\left.+\frac{117}{100\lambda_a^2}\right],\\
C_x &= -\frac{96}{125\pi\,\Delta s^2\lambda_a^4}\left[10-\frac{1}{5}\left(\frac{158}{5}+3\sqrt{5}+\frac{55\sqrt{13}}{13}+\frac{27\sqrt{29}}{29}+\frac{19\sqrt{37}}{37}+\frac{27\sqrt{45}}{45}+\frac{51\sqrt{53}}{53}\right.\right.\\
&\quad\left.\left.+\frac{43\sqrt{61}}{61}+\frac{36\sqrt{17}}{17}+\frac{30\sqrt{85}}{17}\right)\frac{1}{\lambda_a}+\frac{2131}{200\lambda_a^2}\right],\\
C_y &= -\frac{96}{125\pi\,\Delta s^2\lambda_a^4}\left[10-\frac{1}{10}\left(\frac{254}{5}+9\sqrt{5}+\frac{85\sqrt{13}}{13}+\frac{33\sqrt{29}}{29}+\frac{73\sqrt{37}}{37}+\frac{81\sqrt{45}}{45}+\frac{57\sqrt{53}}{53}\right.\right.\\
&\quad\left.\left.+\frac{97\sqrt{61}}{61}+\frac{132\sqrt{17}}{17}+\frac{42\sqrt{85}}{17}\right)\frac{1}{\lambda_a}+\frac{2001}{200\lambda_a^2}\right],
\end{aligned}
\tag{B.3}
$$

for $h_0 = 5\Delta s$.

References

[1] M. Schüssler, D. Schmitt, Comments on smoothed particle hydrodynamics, Astron. Astrophys. 97 (1981) 373–379.
[2] G. Phillips, J.J. Monaghan, A numerical method for three-dimensional simulations of collapsing, isothermal, magnetic gas clouds, Mon. Not. R. Astron. Soc. 216 (1985) 883–895.
[3] J.W. Swegle, D.L. Hicks, S.W. Attaway, Smoothed particle hydrodynamics stability analysis, J. Comput. Phys. 116 (1995) 123–134.
[4] S. Nugent, H.A. Posch, Liquid drops and surface tension with smoothed particle applied mechanics, Phys. Rev. E 62 (4) (2000) 4968–4975.
[5] J.J. Monaghan, SPH without tensile instability, J. Comput. Phys. 159 (2000) 290–311.
[6] J.P. Gray, J.J. Monaghan, R.P. Swift, SPH elastic dynamics, Comput. Methods Appl. Mech. Engrg. 190 (2001) 6641–6662.
[7] Y. Meleán, L. Di G. Sigalotti, A. Hasmy, On the SPH tensile instability in forming viscous liquid drops, Comput. Phys. Commun. 157 (2004) 191–200.
[8] C.T. Dyka, P.W. Randles, R.P. Ingel, Stress points for tension instability in SPH, Internat. J. Numer. Methods Engrg. 40 (1997) 2325–2341.
[9] L.D. Libersky, P.W. Randles, Boundary conditions in a meshless staggered particle code, Technical Report LA-UR-98-590, Los Alamos National Laboratory, Los Alamos, NM, 1998.
[10] G.A. Dilts, Moving least squares hydrodynamics: Consistency and stability, Internat. J. Numer. Methods Engrg. 44 (1999) 1115–1155.
[11] J.K. Chen, J.E. Beraun, C.J. Jih, An improvement for tensile instability in smoothed particle hydrodynamics, Comput. Mech. 23 (1999) 279–287.
[12] J. Bonet, S. Kulasegaram, Correction and stabilization of smoothed particle hydrodynamics methods with applications in metal forming simulations, Internat. J. Numer. Methods Engrg. 47 (2000) 1189–1214.
[13] J. Bonet, S. Kulasegaram, Remarks on tension instability of Eulerian and Lagrangian corrected smooth particle hydrodynamics (CSPH) methods, Internat. J. Numer. Methods Engrg. 52 (2001) 1203–1220.
[14] T. Belytschko, S. Xiao, Stability analysis of particle methods with corrected derivatives, Comput. Math. Appl. 43 (2002) 329–350.
[15] Wm.G. Hoover, C.G. Hoover, E.C. Merritt, Smooth-particle applied mechanics: Conservation of angular momentum with tensile stability and velocity averaging, Phys. Rev. E 69 (2004) 016702-1–10.
[16] J.J. Monaghan, On the problem of penetration in particle methods, J. Comput. Phys. 82 (1989) 1–15.
[17] B.W. Silverman, Density Estimation for Statistics and Data Analysis, Chapman & Hall, London, 1996.
[18] L.I. Sedov, Similarity and Dimensional Methods in Mechanics, Academic Press, New York, 1959.
[19] J. Bonet, T.-S.L. Lok, Variational and momentum preservation aspects of smoothed particle hydrodynamic formulations, Comput. Methods Appl. Mech. Engrg. 180 (1999) 97–115.
[20] A.E. Evrard, Beyond N-body — 3D cosmological gas dynamics, Mon. Not. R. Astron. Soc. 235 (1988) 911–934.
[21] L. Di G. Sigalotti, H. López, A. Donoso, E. Sira, J. Klapp, A shock-capturing SPH scheme based on adaptive kernel estimation, J. Comput. Phys. 212 (2006) 124–149.
[22] R.A. Gingold, J.J. Monaghan, Binary fission in damped rotating polytropes, Mon. Not. R. Astron. Soc. 184 (1978) 481–499.
[23] J.J. Monaghan, Smoothed particle hydrodynamics, Rep. Progr. Phys. 68 (2005) 1703–1759.
[24] L. Hernquist, N. Katz, TREESPH — A unification of SPH with the hierarchical tree method, Astrophys. J. Suppl. Ser. 70 (1989) 419–446.
[25] J.J. Monaghan, SPH compressible turbulence, Mon. Not. R. Astron. Soc. 335 (2002) 843–852.
[26] L.B. Lucy, A numerical approach to the testing of the fission hypothesis, Astron. J. 82 (1977) 1013–1024.
[27] L.D. Landau, E.M. Lifshitz, Statistical Physics, vol. 5, Addison-Wesley Publishing Company, Reading, Massachusetts, 1969.

[28] J.P. Morris, Simulating surface tension with smoothed particle hydrodynamics, Internat. J. Numer. Methods Fluids 33 (2000) 333–353.
[29] J. Swegle, SPH in tension, Memo, Sandia National Laboratories, Alburqueque, NM, 1992.
[30] M. Omang, S. Børve, J. Trulsen, SPH in spherical and cylindrical coordinates, J. Comput. Phys. 213 (2006) 391–412.
[31] M. Shashkov, B. Wendroff, A composite scheme for gas dynamics in Lagrangian coordinates, J. Comput. Phys. 150 (1999) 502–517.